MULTIPLE-POINT GEOSTATISTICS TO DERIVE MISSING SURFACE DISPLACEMENT VALUES OF A GLACIER INFERRED FROM DINSAR

BHUWAN RANJIT
February, 2017

SUPERVISORS:
Dr. V. A. Tolpekin
Prof. Dr. Ir. A. Stein

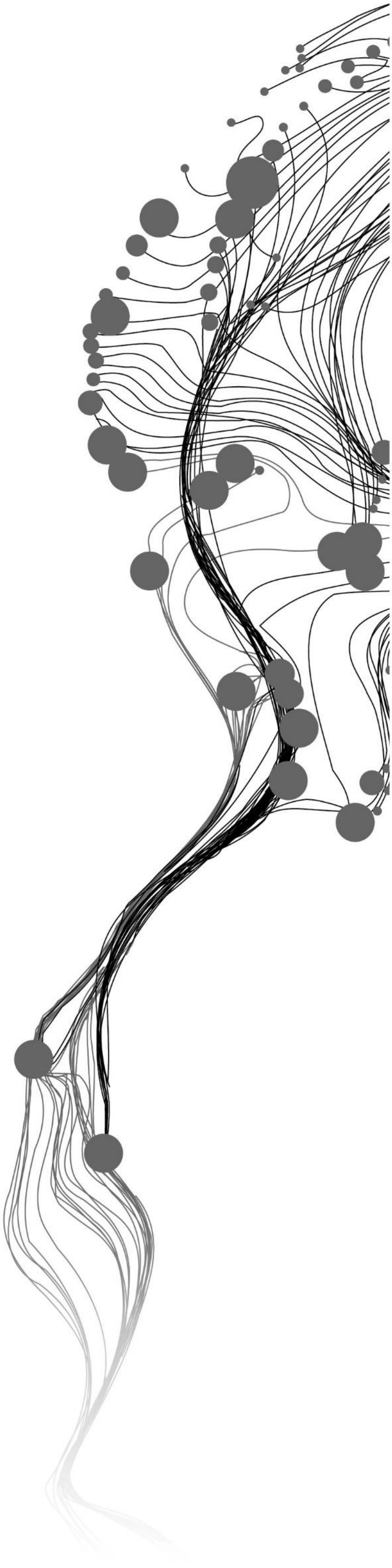

MULTIPLE-POINT GEOSTATISTICS TO DERIVE MISSING SURFACE DISPLACEMENT VALUES OF A GLACIER INFERRED FROM DINSAR

BHUWAN RANJIT

Enschede, The Netherlands, [February, 2017]

Thesis submitted to the Faculty of Geo-Information Science and Earth Observation of the University of Twente in partial fulfilment of the requirements for the degree of Master of Science in Geo-information Science and Earth Observation.

Specialization: Geoinformatics

SUPERVISORS:
Dr. V. A. Tolpekin
Prof. Dr. Ir. A. Stein

THESIS ASSESSMENT BOARD:
Prof. Dr. Ir. M.G. Vosselman (Chair)
Dr. M. Oesting (External Examiner, University of Siegen)

ABSTRACT

Glacier displacements play a vital role in the monitoring and understanding of glacier dynamics. Glacier displacement fields are typically retrieved from pre- and post-event SAR images using DInSAR. The glacier displacement map produced by DInSAR contains missing values due to decorrelation of the SAR images. This study demonstrates the utility of multiple-point geostatistics to reconstruct these missing values. Amongst several well-established multiple-point geostatistics methods, direct sampling is used for deriving those missing values. Univariate and bivariate implementations of direct sampling are employed. In the univariate implementation, missing values are derived in single displacement map, whereas in bivariate implementation gaps in two displacement maps are filled simultaneously. Evaluation is carried out by artificially generated missing values on the displacement map of different shapes and sizes at different locations with known values. Imposed missing values are then reconstructed and compared with the original values. Reconstruction results of the two direct sampling implementations were compared with ordinary kriging using the RMSE, a histogram of the residuals, scatterplots and the residual distribution map. The study shows that with an increase in the size of such discontinuities, ordinary kriging predictions deteriorate significantly, whereas only slight decrease in reconstruction accuracy is observed for direct sampling. The results of both direct sampling implementations are similar. The univariate implementation shows a slight performance increase as compared to the bivariate implementation because the information from the ancillary data is only partly complementary to enhance bivariate reconstructions. Direct sampling performed better than ordinary kriging with accuracy below the DInSAR detection limit. The study concludes that multiple-point geostatistics is an effective method for deriving missing values in a DInSAR derived displacement map. Direct sampling based reconstruction is straightforward to implement and parameters can be fine-tuned with minimum user intervention.

Keywords

Glacier displacements, DInSAR, Kriging, Multiple-point geostatistics, Direct sampling

ACKNOWLEDGEMENTS

First of all, I would also like to express my sincere gratitude to my supervisors, Dr. V. A. Tolpekin and Prof. Dr. Ir. A. Stein, for their critical analysis, feedbacks, guidance, suggestions and encouragement throughout the thesis period. Without their guidance, this work would not have come to this form.

I would like to thank Netherlands Fellowship Programmes (NFP) for granting me the scholarship to pursue my M. Sc. degree at ITC. I am also thankful to my employer, Ministry of Land Reform and Management, Government of Nepal, for allowing me an opportunity to study in ITC on study leave.

I am grateful to Gregoire Mariethoz, Philippe Renard and Julien Straubhaar for providing the DeeSse software for this academic research. Especial thanks to Julien Straubhaar, University of Neuchatel, for providing technical guidance on the software. I also deeply appreciate the help from all the authors of different literatures for answering my queries on the subject.

I am thankful to my friends for keeping me moving forward. Finally, I would like to express my thanks to my family back home and my extended family here, Enschede Nepali Family, for their continuous support and encouragement throughout the study.

TABLE OF CONTENTS

LIST OF FIGURES

LIST OF TABLES

LIST OF ABBREVIATIONS

AOI	Area of Interest
CCSIM	Cross Correlation based Simulation
CIQ	Conditional Image Quilting
CK	Co-kriging
DeeSse	DS: Multiple-Points Simulation by Direct Sampling
DEM	Digital Elevation Model
DInSAR	Differential Interferometric Synthetic Aperture Radar
DS	Direct Sampling
DS_b	Direct Sampling Bivariate Simulation
DS_u	Direct Sampling Univariate Simulation
DTAR	Distributed Target Ambiguity Ratio
ESA	European Space Agency
EW	Extra Wide Swath Mode
GLOF	Glacier Lake Outburst Flood
GRD	Ground Range Detection
IDW	Inverse Distance Weighting
IK	Indicator Kriging
InSAR	Interferometric Synthetic Aperture Radar
IQ	Image Quilting
IW	Interferometric Wide Swath Mode
LOS	Line of sight
MCF	Minimal Cost Flow
MLC	Maximum Likelihood Classification
MPS	Multiple Point Geostatistics
MRF	Markov Random Field
NESIM	Normal Equation Simulation
OK	Ordinary Kriging
POD	Precise Orbit Determination
RBF	Radial Basis Function
RCM	Regional Climate Model
RF	Random Function
RMSE	Root Mean Square Error
S1	Sentinel-1
SAR	Synthetic Aperture Radar
SG	Simulation Grid
SGeMS	Stanford Geostatistical Modeling Software
SLC	Single Look Complex
SM	Stripmap Mode
SNAP	Sentinel Application Platform
SNESIM	Single Normal Equation Simulation
SNR	Signal to Noise Ratio
SRTM	Shuttle Radar Topography Mission
TI	Training Image
TIN	Triangulated Irregular Network

TOPSAR	Terrain Observation with Progressive Scans SAR
UK	Universal Kriging
UTM	Universal Transverse Mercator
WGS	World Geodetic Co-ordinate System
WV	Wave Mode

1. INTRODUCTION

1.1. MOTIVATION AND PROBLEM STATEMENT

Mountain glaciers, an integral part of the cryosphere, cover 10 % of Earth's surface and play a vital role in Earth's natural system (Leibowitz, 2009). They are an important source of fresh water to downstream population and glacier melt contributes to the river flow. In mountains surrounded by arid plains, meltwater from the glaciers are crucial for use in irrigation (Petrakov et al., 2016). They serve as the main indicator of climate change. Global temperature increase is causing glacier retreat in an alarming rate and some are on the verge of disappearance (Kaltenborn et al., 2010). Due to glacier retreat, unstable lakes are formed, which burst when triggered by earthquakes, landslides and avalanche. Such Glacier Lake Outburst Floods (GLOFs) claim lives of many and destroy agriculture and infrastructures such as hydropower, and roads. Nepal alone has suffered 15 GLOFs during the last century (Richardson & Reynolds, 2000), for example, the Dig Tsho GLOF of 1985 (Mool et al., 2011). Therefore, mapping glacier extent and monitoring temporal changes are essential for planning and management of water resources.

Glaciers are masses of ice formed by the accumulation and compaction of snow over a long duration of time. They constantly move because of stresses induced by their weight and gravity. Information on glacier velocity is essential for studying the glacier dynamics and is required for verification of models dealing with this subject. Glacier surface velocity is a vital part of the mass balance models and therefore, glacier surface velocity determination is important for monitoring the glacier response to climate change (Wangensteen et al., 2005). Further, glacier velocity helps to understand the internal stresses and strains caused by gravity-induced flow (Joughin et al., 2010). Glacier velocity is also necessary for better knowledge of seasonal variability, acceleration and deceleration of glaciers (Wuite et al., 2015) and hazard prediction (Quincey et al., 2007). Hence, there is a dire need for monitoring and assessing the glacier velocity.

The most accurate and reliable method of glacier velocity measurement is to conduct in situ measurements. But these methods are costly, time-consuming and limited over a small geographical area. Furthermore, these methods are impractical to perform regularly due to the inaccessibility, remoteness and vastness of the mountain glaciers. Thus, satellite remote sensing is an effective and efficient technique for deriving surface velocity of glaciers (Joughin et al., 2010; Wangensteen et al., 2005).

For many years, feature tracking in optical sensors has been exploited for deriving glacier velocity remotely. But cloud cover in this imagery, especially in the mountainous region, is a major problem limiting its use (Kääb, 2005; Li et al., 2004). Recently developed microwave remote sensing systems eliminate this limitation for surface velocity determination because they are independent of sun-illumination, penetrate cloud and can function day and night in all-weather condition (Lee et al., 2009).

From Synthetic Aperture Radar (SAR) images, SAR interferometry and feature tracking are two extensively used techniques to determine glacier velocity. SAR interferometry is capable of providing velocity estimates at any point on the glacier, whereas feature tracking relies on detectable surface features in the both images and fails in the area where distinct surface features like crevasses are not present (König et al., 2001). In addition, temporal baseline of few days between the images is applied for InSAR, while feature tracking uses longer repeat-pass periods, usually a year between the images (König et al., 2001; Luckman et al., 2007)—but will not be able to characterize seasonal surface velocity of glacier. Another constraint of feature tracking is that its detection limit depends on the pixel size of the SAR images (González et al., 2009). Above all, glacier displacement estimates from the SAR interferometry is considerably more accurate and precise—in the order of few centimetres—compared to feature tracking. Thus, InSAR technique is greatly valued for glacier velocity studies.

SAR interferometry uses the phase information of the radar images of the same scene acquired from two positions using two receiving antennas. The two SAR images must be coherent to form interferogram which comprises phase difference information. The two receiving antennas are either separated in time (repeat pass acquisition) or space (along-track or across-track acquisition). Since most of the SAR sensors provide images of same scene acquired at some time apart, repeat pass SAR interferometry has been widely used and proven to be suitable technique for glacier surface velocity estimation. For the first time, Goldstein et al. (1993) successfully mapped glacier surface velocity of the Rutford Ice Stream, Antartica by combining two SAR images with 6-day separation. Since then, many researchers have extensively applied InSAR technique to retrieve the glacier velocity (König et al., 2001; Massonnet & Feigl, 1998; Rott, 2009; Schneevoigt et al., 2012; Wangensteen et al., 1999; Wangensteen et al., 2005).

Temporal decorrelation is the major factor limiting the use of InSAR caused by snow and ice melting, wind induced snow drift, precipitation in form of snow or rain and gradient of displacement greater than half a fringe per pixel (Strozzi et al., 1999; Strozzi et al., 2002; Zebker & Villasenor, 1992). Thus, time interval between acquisitions is crucial to preserve coherence between the SAR image pair. Few studies attempted to use image pairs of longer time interval such as Mohr & Madsen (2000) tried ERS-1/2 with 35 days temporal baseline in Greenland glaciers, Joughin et al. (1999) attempted RADARSAT-1 having time interval of 24 days ice sheet of West Antartica and Strozzi et al. (2008) used JERS-1 having time interval of 44 days in East Antartica. But in these studies, decorrelation was observed mainly in areas of rapid flow. For these reasons, scenes from ERS-1 and ERS-2 with one or three days temporal baseline during ice mission in 1992 and 1994, and tandem phase from 1995 to 2000 were widely used for mapping glacier movement, but these missions are no longer in operation. Amongst current satellite sensors, Sentinel mission is the latest and most promising source for repeat pass SAR data. Sentinel-1 (S1) is C-band SAR system built on heritage SAR systems of European Space agency (ESA)'s ERS-1, ERS-2 and Envisat, and Canada's Radarsat-1 and Radarsat-2, with enhanced reliability, revisit time, geographical coverage and rapid data dissemination (ESA, 2013a).

The first S1 satellite (S1-A) was launched on 3 April 2014 followed by second (S1-B) on 25 April 2016 completing the S1 constellation (ESA, 2014). S1-A provided 12 days repeat image pair, which shortened to 6 days once S1-B became operational. S1 image pair of 6 days temporal baseline is an excellent dataset compared to 35 days image pair from Envisat. This decrease in time interval between the acquisitions of the two S1 images reduces the constraint of temporal decorrelation. Thus, the prospect of using freely available S1 data for InSAR is promising and has been explored in this study. The enhanced interferometric capability of S1 is a reliable source for glacier monitoring. In addition, seasonal patterns can be assessed as huge sets of S1 SAR data are available.

Coherence serves as an indicator of how good an interferogram is. The quality of an interferogram formed from co-registered SAR image pair is characterized by coherence. Loss of coherence produces unreliable interferometric results. Thus, the area with low value of coherence should be avoided and are masked out during phase unwrapping process (Schneevoigt et al., 2012).

As a consequence, the glacier surface displacement map derived from InSAR consists of missing values (gaps) in incoherent areas. Reconstruction of these spatial discontinuities is of high importance in glacial studies for example: to integrate these data with modelling frameworks requiring continuous data fields (Mariethoz et al., 2012), to assess the spatial and temporal patterns of the glacier displacement (Mair et al., 2001; Persk et al., 2004) and to locate supraglacial lakes (Quincey et al., 2007).

Several popular approaches available for gap-filling can be categorized into either deterministic or geostatistical interpolation methods. In the deterministic techniques, mathematical functions are used to interpolate the values at unsampled location, based on either the degree of similarity (for example: Inverse Weighted Distance (IDW)) or the degree of smoothing (for example: Radial Basis Function (RBF)) in relation with neighbouring data points (Peralvo & Maidment, 2003). However, these deterministic methods are unable to provide uncertainty estimates. Geostatistical methods are based on statistical models performing stochastic predictions of values at unknown locations, and therefore can provide spatial model of uncertainty or estimates of prediction accuracy (Johnston et al., 2001).

In several studies, kriging, a parametric geostatistical approach, has been used to fill gaps (Zhang et al., 2012). Zhang et al. (2009) applied this method to fill gaps in multispectral images by imposing correlation with the gap free image acquired four months before. However, traditional geostatistics is based on Random Function (RF) model parameterized by semi-variogram and covariance. Therefore, spatial variability is captured by only considering two spatial locations at one time. This results in smoothing effect and only considers linear relationship with covariates (Goovaerts, 1997). So, the spatial dependency of phenomenon exhibiting a much stronger correlation at higher order cannot be described by two-point statistics (Mariethoz & Caers, 2015). This is why traditional geostatistics fail to reproduce geometries of curvilinear structures, such as meandering river channels, incised valleys etc. (Strebelle, 2002). Recently developed Multiple-point geostatistics (MPS) method, belonging to family of non-parametric geostatistical methods, can solve this problem because spatial variability is modelled using training images (TIs), from which spatial structures and patterns are borrowed (Strebelle, 2002).

Thus, it is necessary to study the possibility of the reconstruction of the gaps caused by loss of coherence in InSAR derived displacement maps of glaciers and predict the missing data by using MPS.

1.2. RESEARCH IDENTIFICATION

Use of S1 image pair in the Himalayan glacier has not been studied so far, although there has been extensive research regarding SAR interferometry for glacier displacement determination. Recently, Sentinel has received much attention in glacial applications. This research aims to investigate the potential of S1 image pairs for glacier displacement studies in the Himalayas. S1 datasets are freely available and rich, and they are the most economical and promising data source for long-term glacier monitoring, especially for developing countries around the Himalayas.

To our best knowledge, no research has been carried out yet to apply MPS for predicting the missing values in gaps caused by incoherent data in InSAR derived glacial surface displacement map. Therefore, in this research MPS approach shall be investigated for filling up those gaps to obtain glacial surface displacement map without any spatial discontinuities.

1.3. RESEARCH OBJECTIVES

The main objective of this research is to implement multiple-point geostatistics (MPS) to derive the missing surface displacement values of a glacier inferred from DInSAR. This is achieved through the following specific objectives:

1. To review, evaluate and select a MPS method that reproduces the pattern both complex and small-scale in the gaps of glacier surface displacement map derived from DInSAR.
2. To perform pattern reconstruction in the gaps by implementing the chosen MPS method.
3. To assess the reconstructed results of the missing values in the glacier surface displacement map.
4. To compare the performance of the MPS gap filling against conventional geostatistical method.

1.4. RESEARCH QUESTIONS

For the fulfilment of the aforementioned objectives, the following research questions are formulated:

1. Which MPS method is most suitable to reconstruct the missing surface displacement values inferred from DInSAR?
2. What are the optimal parameter settings for implemented MPS method to obtain the best pattern reproduction?
3. How fully informative training images (TIs) can be made for reconstruction of pattern and spatial structure in the gaps?
4. What are the effective methods for assessment of the reconstructed results in the missing area?
5. Which conventional geostatistical method is appropriate for benchmarking the MPS results?
6. Does MPS perform better gap filling compared to the conventional geostatistical method? If yes, in which aspect of performance measures is MPS superior to conventional geostatistical method?

1.5. INNOVATION AIMED AT

This research shall be carried out to derive the surface displacement of Himalayan glacier, one of the toughest topography, from novel S1 SAR data applying SAR interferometry technique. Most importantly, S1 data are available free of charge (ESA, 2013). So, the exploration of this novel dataset for glacial monitoring is promising.

The other novelty of this research is aimed at reconstruction of gaps in the glacier displacement maps derived from InSAR technique using MPS. An appropriate MPS algorithm shall be chosen and used to reproduce the complex patterns and spatial structure in the missing area of glacial surface displacement map which traditional two-point geostatistical methods are unable to reconstruct. Finally, the accuracy of the reconstructed gaps shall be evaluated.

1.6. THESIS OUTLINE

The structure of the thesis is outlined here. It is divided in 7 chapters. Chapter 1 introduces the motivation, problems, objectives, questions and innovations of this research work. In Chapter 2, review of DInSAR technique, their applications in glacier studies and the existing problem focusing on S1 dataset are presented. Then, Chapter 2 continues with the review of several MPS algorithms and their potential to solve the problem at hand. At the end of Chapter 2, the chosen MPS algorithm to be implemented for gap filling is described. Chapter 3 deals with the information about the study area, the data and software. Chapter 4 explains the methodology adopted for DInSAR and MPS. Chapter 5 presents the results of the work done. The discussion of the findings from the implementation, accuracy assessment and comparative analysis conducted as given in Chapters 6. Finally, Chapter 7 concludes with insights gained from the research, addresses the research questions and recommendations for the future research.

2. LITERATURE REVIEW

This chapter presents a brief review of SAR interferometry and MPS. The first section focuses on the fundamentals of SAR interferometry, its applications in glaciology, potential of S1 interferometry to derive glacier surface displacements and missing values in DInSAR derived displacement maps caused by decorrelation in InSAR. The second section describes briefly the background of MPS, existing MPS algorithms and the selected MPS algorithm to be implemented for reconstructing gaps in the LOS displacement map. At last, a conventional geostatistical method chosen to benchmark the MPS reconstruction is explained.

2.1. SAR INTERFEROMETRY

SAR data have been successfully applied in earth sciences for more than 20 years. One of the characteristic that makes SAR systems stand out is their capability to acquire images both day and night, and in all weather conditions. This is because SAR sensors are active microwave remote sensing systems. SAR sensor illuminates targets on the earth surface by transmitting a series electro-magnetic microwave pulses. The SAR sensor extracts information about illuminated target by measuring the reflected radar echoes. The received signal are complex having both amplitude and phase information. The amplitude is a measure of strength of the backscattered signal and is characterized by the geometrical properties of the target, while the phase is record of the fraction of last wavelength received by the SAR sensor.

In SAR interferometry (also known as Interferometric Synthetic Aperture Radar (InSAR)), the phase difference between two SAR images acquired from a slightly different position at different times are used to determine surface topography and the displacement on the earth's surface (Massonnet & Feigl, 1998). The two different InSAR techniques used are: single-pass SAR interferometry and repeat-pass SAR interferometry.

In single-pass interferometry, two SAR images are simultaneously acquired from two antennas/receivers mounted on a single platform separated by a known distance called baseline. Whereas, repeat-pass interferometry involves two images of the same area being acquired by a single antenna in different passes of the satellite. In the former technique, there is no temporal separation between two acquisitions referring no surface deformation between the two images; leaving only topographic component in the phase difference. So, this technique is mostly used for creating high resolution digital elevation models (DEMs) because of less error than repeat-pass (Zhong et al., 2003). For example: there is no error caused by atmospheric variation in single-pass, whereas any change in atmospheric condition between two acquisitions affects repeat-pass. The single-pass interferometry was first used by Zebker & Goldstein (1986) for topographic mapping. Famous implementation of single-pass interferometry is the space borne Shuttle Radar Topography Mission (SRTM), which generated global high-resolution topographic data (Farr & Kobrick, 2000). In the latter technique, the antenna position is spatially as well as temporally separated between the two acquisitions, so the phase difference has contribution from both surface topography and possible surface displacement. Thus, the repeat-pass interferometry involves removing the topographic phase contribution to obtain the displacement that may have occurred between the two acquisitions (Rosen et al., 2000). This approach is generally referred to as differential InSAR (DInSAR) and has the potential to detect ground deformation with millimetre to centimetre scale precision. DInSAR was first demonstrated by Gabriel et al. (1989) to detect the earth's surface displacement of many geophysical phenomena such as swelling and buckling in fault zones, displacement caused by earthquake and volcanic activities. Repeat-pass interferometry is the typical implementation for most of the satellite based sensors such as ERS-1, ERS-2, JERS-1, Radarsat and Envisat. Sentinel-1 also functions in repeat-pass mode which is why repeat-pass interferometry technique has been utilized in this research.

In DInSAR approach, one can take three images and construct two interferometric phase measurements. One image pair is considered to contain only the topographic signature, while the other pair comprises of both topography and surface displacement. The topographic contribution obtained from first pair is deducted from second such that the resulting interferometric phase is only from surface deformation (Rosen et al., 2000). Instead of 3-pass DInSAR, when only two SAR images are available, an external DEM can be used to deduct the topographic phase to obtain surface deformation between the two acquisitions (Schneevoigt et al., 2012). Since the temporal resolution of S1 is of 6 days, all image pairs on the glacier will contain both topographic and surface displacement signature. Thus, 2-pass DInSAR with external DEM is the implementation used in this research.

2.1.1. DInSAR application in glaciology

The ESA's first SAR mission ERS-1 was launched in 1991, which gathered large amount of data over wide area of the globe. This triggered the application of InSAR in earth sciences to study surface deformation due to volcanic eruption (Amelung et al., 2000; Massonnet et al., 1995), earthquakes (Massonnet et al., 1993; Massonnet & Feigl, 1998) and landslides (Berardino et al., 2002; Colesanti & Wasowski, 2006; Hilley et al., 2004; Rott & Nagler, 2006). Further applications of InSAR are in hydrology for soil moisture monitoring (Makkeasorn et al., 2006; Smith et al., 2000) and water level measurement and monitoring in lakes and reservoirs (Alsdorf et al., 2001; Romeiser et al., 2007; Wdowinski, 2004), in forestry for canopy height estimation which is used to quantify the forest biomass (Askne et al., 1999; Balzter et al., 2007; Wegmüller & Werner, 1997). Goldstein et al. (1993) pioneered the application of DInSAR in glacier monitoring by successfully applying ERS-1 images for glacier displacement of Antarctic ice stream over 6 days between the images. After him, several scientists have successfully implemented DInSAR technique for glacier studies.

The ERS-1 ice phase data acquired during 3-day repeat orbit (1992 and 1994) opened up the opportunity of using DInSAR for glacier studies with reduced temporal separation. One of the publications dealing with three days interferometry with glacier displacement applications is by Strozzi et al. (2002). The ESA ERS-2 launched in 1993 is an identical satellite system to ERS-1, which allows interferometry between them. The ERS-1/-2 tandem mission operated only in 1995/1996 and provided SAR images of 1 day repeat-pass data. Because of which ERS-1/-2 tandem images were the most exploited data source for glaciological analysis. Several researchers have carried out 2-pass DInSAR for glaciological studies using ERS-1/-2 tandem images (Eldhuset et al., 2003; Rott, 2009; Schneevoigt et al., 2012; Wangensteen et al., 1999; Wangensteen et al., 2005).

The glacier velocity derived from SAR interferometry can help in identifying the causes of the ice shelf acceleration (Vieli et al., 2007). The displacement and velocity field of glaciers obtained through SAR interferograms has been used successfully to monitor uplifting (Jónsson et al., 1998) and infilling (Björnsson et al., 2001) of the ice cauldrons, estimating snow accumulation (Oveisgharan, 2007), motion patterns (Li et al., 2008), redistribution patterns of wind-drifted snow (Li & Sturm, 2002), glacier surface topography (Joughin et al., 1996; Kwok & Fahnestock, 1996; Mohr et al., 1998), mass flux (Rott et al., 1998), surface lowering of the glaciers (Muskett et al., 2008) and glacier surges (Fischer et al., 2003). Gray et al. (2005) used vertical displacement field derived from SAR interferometry to infer subglacial water movement. Furuya & Wahr (2005) inferred the water level change of supraglacial lakes by assessing height changes from the DEMs derived from InSAR. Joughin et al. (1998) and Mohr et al. (1998) derived 3-dimentional glacier velocity using ascending and descending passes assuming flow parallel to the surface.

ERS-1/-2 tandem images have been widely used for glacier studies in Himalaya range. Kumar et al. (2008) studied the movement of the two Himalayan glaciers: Siachen and Gangotri using ERS-1/-2 images. The surface velocities of the two famous glaciers in Everest region of Himalayan range—Khumbu and Kangshung were derived from ERS-1/-2 images applying DInSAR technique by Luckman et al. (2007). Quincey et al. (2007) demonstrated the potential of SAR interferometry derived glacier velocity for early detection of the potential glacial lake hazards in Himalayan glacier. The study area covered five glaciers in the Tama Koshi and Dudh Koshi river basins and showed that development of the lakes in the debris-covered tongue takes place in stagnant region with displacement less than 5 m a^{-1}. Quincey et al. (2009) applied DInSAR approach derived glacier surface velocity to extract information on the stagnation extent which is an indicator of glacier retreat in 20 glaciers across the Everest region of Himalayas.

ERS-1/2 SAR images were excellent dataset for InSAR glacier studies, but they are no longer operational. For the continuity of C-band SAR data, S1 was built on ESA's and Canada's the heritage SAR systems namely ERS-1, ERS-2, Envisat and Radarsat (ESA, 2014). S1 mission has been optimized for InSAR application. At present, S1 is the satellite mission providing global open data with short repeat acquisition plan of 6-day. Thus, with this newest SAR mission, researchers are presented huge opportunities to explore S1 data for various InSAR applications, including glacier study which is this research's application of interest.

2.1.2. Potential of S1 interferometry to derive glacier surface displacements

Several scientists have investigated the potential of C-band SAR mission with 12 days repeat-pass—Sentinel-1—to derive glacier surface velocity using DInSAR. Before the launch of S1 mission, equivalent ERS-1/2 C-band SAR data was used to study the future prospect of S1. Strozzi et al. (2007) used ERS-1 ice mission data with 3-day repeat orbits acquired in 1992 and 1994 at Nordaustlandet and computed five 12 days interferograms. They successfully derived LOS surface displacement maps out of two coherent interferograms.

Interferometric wide (IW) swath mode is the standard acquisition mode over land. Yague-Martinez et al., (2016) provided recipe-like description of interferometric processing of S1 IW data and demonstrated the interferometric capabilities of S1 data for geophysical applications. Similarly, Prats-Iraola et al. (2015) investigated the interferometric performance of S1 IW 12-day repeat pass data over glacier scenario and demonstrated excellent results over a Greenland glacier. All these studies confirm the promising interferometric capabilities of the S1 data acquired in IW mode for glacier displacement studies.

For mountain glaciers, short repeat acquisitions are desired because of their larger deformation rates compared to Greenland and Antarctic ice sheets (Berthier et al., 2005; Li et al., 2008). After the launch of S1 B on 25 April 2016, the S1 constellation is complete. The two satellites S1 A and B fly in coordinated orbits delivering 6-day repeat pass images with improved coverage. The 6 day repeat pass images provides much better interferometric results than the 12 day repeat pass images by reducing temporal decorrelation. S1 provides dense time series of free SAR data with shorter repeat cycle compared to previous SAR missions (for example: 35 day for Envisat). Thus, it is worthwhile to investigate potential of S1 data to deriving surface displacement field of Himalayan glacier.

2.1.3. Decorrelation in InSAR

InSAR works only under coherent conditions. Coherence is the complex correlation coefficient of two complex SAR images. The values of coherence are within the range of [0, 1], where 0 indicates completely decorrelated signals and 1 refers to perfectly correlated signals. Coherence is an indicator of the quality of interferogram. Low coherence value produces unreliable interferometric results.

The changes in the position or the properties of the backscattering elements over the time span between the SAR acquisitions results in the decrease of the coherence value. The main causes of the temporal decorrelation are meteorological events such as snowfall and rainfall, wind induced surface snow redistribution, and melting of snow and ice (Strozzi et al., 1999; Strozzi et al., 2002; Zebker & Villasenor, 1992). Another restriction for the application of InSAR arises due to it's the displacement gradient threshold. The displacement gradient threshold of InSAR is half a fringe per pixel. When the surface displacement is greater than the threshold, the individual phase cycles cannot be resolve. Thus InSAR technique fails in zones of strong displacement gradient (Nagler et al., 2015; Zhou et al., 2009).

Additional source of decorrelation is the mismatch in the properties of the two imaging systems caused by volumetric scattering, processing errors, large interferometric baseline (i.e. perpendicular baseline greater than critical baseline) and geometric (orbit errors). Due to high penetration of the SAR signals in the snow and ice of glaciers, volumetric decorrelation occurs (Langley et al., 2007). Processing error can be avoided by applying correct processing chain. For S1, precise orbit parameters are provided by ESA. Based on the precise orbit data, the geometry is more accurate which eliminates the geometric errors (for example: accurate coregistration of the two SAR images) (Gens & Genderen, 1996). The S1 orbit maintenance strategy ensures small perpendicular baseline on the order of 150 m (Yague-Martinez et al., 2016). Thus, the perpendicular baseline is smaller than the critical baseline. The decorrelation caused by interferometric baseline are negligible due to small baseline between the interferometric acquisitions (Tamm et al., 2016). The complete discussion on the sources of loss of coherence are presented in Hanssen (2001).

Since phase noise and decorrelation degrades the phase accuracy in SAR interferometry, the phase in areas with low coherence values should not be unwrapped (Li et al., 2008). The incoherent areas are masked out and are excluded in the further analysis – conversion of unwrapped phase to surface displacement. Thus, InSAR derived glacier surface displacement map comprises of missing values in the areas of insufficient coherence. It is necessary to fill these spatial discontinuities in order to obtain continuous displacement field for glacier studies like assessing spatial and temporal pattern of glacier displacement, integration with modelling frameworks requiring continuous data, glacier hazard monitoring and glacier dynamics.

2.2. MPS ALGORITHM SELECTION

2.2.1. Background of MPS

An appropriate method of interpolation is needed to fill missing values in the surface displacement map. Traditional geostatistical methods were applied for several gap filling studies (Zhang et al., 2012). They are based on the variogram modelling to capture the spatial heterogeneity. For this reason, they are limited to reproduction of the two-point statistics. Most natural phenomenon however, exhibit higher order dependencies. The inability of the variogram based model to capture continuity of actual phenomena have been pointed out by Caers & Journel (1998) and Strebelle (2002). As remedy to the limitations of traditional two-point geostatistics, Guardiano & Srivastava (1993) introduced MPS. They proposed to use non parametric TIs instead of variogram to obtain prior spatial model. TIs are grids consisting of the spatial patterns deemed representative of the spatial structures being simulated. The use of TIs makes it possible to consider correlation between multiple spatial locations at a time. As a result, MPS is able to replicate the heterogeneity of spatial phenomenon such as curvilinear and/or connected geometries.

Serious drawbacks known as smoothing effect inherent in the interpolation results obtained from traditional geostatistical approaches such as IDW and kriging (Rezaee et al., 2012; Yamamoto, 2005). Because of the smoothing effect, estimated histogram is narrower than the sample histogram, meaning the low values are overestimated and the higher values are underestimated during estimation process. Hence, spatial variability given by the sample variogram is not reproduced by these traditional geostatistical methods. The conditional simulations are recognized alternative for reproducing the histogram and semivariogram model. MPS is a conditional simulation method so guarantees the global accuracy. MPS can be used to generate multiple equiprobable stochastic realizations of the phenomenon under study. Thus, estimates of uncertainty can be obtained.

It is necessary to capture the magnitude and patterns in spatial variability occurring in the surface displacement field for accurate reconstruction of the missing values in surface displacement map. MPS is considered an emerging solution to the drawbacks inherent in traditional geostatistical methods. Thus, it is opportunistic to investigate if MPS is able to reproduce realistic spatial continuity and higher order statistics.

2.2.2. MPS algorithms

During the last decade, several MPS algorithms have been developed and further, new ones are being proposed regularly. These MPS algorithms can be broadly categorized into two classes either pixel-based or patch-based. In pixel-based algorithms each pixel is simulated one by one sequentially. While, in patch-base algorithm, entire patch of certain size is simulated by quilting simulation values that are next to each other in TI. Therefore, patch-based methods are computationally faster than the pixel-based methods.

The first MPS algorithm called Normal Equation Simulation (NESIM) developed by (Guardiano & Srivastava, 1993) belonged to the family of pixel-based algorithms. This algorithm was inefficient and impractical because entire TI was scanned at each simulation step. These problem were solved by another pixel-based method called Single Normal Equation Simulation (SNESIM) algorithm (Strebelle, 2002). This method proceeds by scanning the entire TI for patterns of a certain template size and their statistics (frequency) were stored in the tree. Afterwards, when the simulation process starts, conditional probabilities at each node is rapidly computed from the search tree. Consequently the computational cost of SNESIM is tremendously reduced compared to NESIM. As a result SNESIM is popular MPS algorithm. Another reason for SNESIM being widely used is because of its free availability in Stanford Geostatistical Modeling Software (SGeMS). Many MPS algorithms essentially similar to SNESIM have been proposed. Straubhaar et al. (2011) developed IMPALA by replacing the search tree in SNESIM with list to store the spatial pattern. Another algorithm based on SNESIM is HOSIM, in which spatial cumulants are used to store patterns instead of frequencies in search tree (Mustapha & Dimitrakopoulos, 2011). GROWTHSIM is another MPS algorithm similar to SNESIM, only difference is that it applies a random-neighbour path (Eskandari & Srinivasan, 2008). Peredo & Ortiz (2011) developed simulated annealing pixel-based algorithm. Apart from SNESIM, direct sampling (DS) is another popular pixel-based MPS algorithm developed by Mariethoz et al. (2010).

The first patch-based method is FILTERSIM proposed by Zhang et al. (2006). Other techniques based on pasting patches are image quilting (IQ) (Efros & Freeman, 2001), SIMPAT (Arpat & Caers, 2007), Patchwork Simulation (El Ouassini et al., 2008), Cross Correlation based Simulation (CCSIM) (Tahmasebi et al., 2012) and Conditional Image Quilting (CIQ) (Mahmud et al., 2014).

2.2.3. Direct Sampling algorithm

The factor that distinguishes DS from other existing MPS algorithms is that instead of counting and storing the patterns found in TI, TI is directly sampled in a random order but conditional to the data events. For simulating a node, the algorithm randomly scans the TI until the pattern in TI is matched with the pattern retrieved from the simulation grid (SG) centred at node to be simulated. Once the match is found, the central node value from the TI is copied and pasted to the node being simulated in SG. The match between two patterns is computed using distance. Due to this basic distance-based simulation principle, DS has become a very flexible method with several advantages over other MPS algorithms.

SNESIM employs storage based on the tree structure which ensures computational efficiency while the tree structure is replaced by list-based catalogue in IMPALA which reduces memory requirement. Use of the pattern database limits these algorithms to consider only categorical variable with few classes and patterns of fixed size. Even though multi-grid approach can be employed to capture large structure, these methods become memory extensive because of use of large template size.

As DS does not need to construct pattern database, both categorical and continuous variables can be simulated by defining appropriate distance between data events based on the type of variable under study. Similarly, another strong feature of DS is that it offers both univariate and multivariate simulations. In multivariate framework, different categorical and continuous variables can be co-simulated preserving the linear as well as non-linear dependencies between simulated variables. This opens door to diverse applications—categorical variables such as geology, soil type, land cover classes etc. and continuous variables such as rainfall, concentration, etc. Apart from potential applications, DS is superior over traditional MPS techniques in terms of computational efficiency. DS algorithm does not store the occurrences of data events. Thus, the memory usage is tremendously reduced and large neighbourhood searches can be performed for reconstruction of large spatial structures. Further, DS efficiently capture large scale structure without using multi grid approach by varying the geometry of the patterns during the simulation itself.

The patch-based MPS algorithms which do not rely on both the pattern database and multigrid are CCSIM and CIQ. In CCSIM algorithm, overlapping patches are pasted along a simulation path by minimizing a cross-correlation function in the overlapping region (Tahmasebi et al., 2012). CIQ pastes overlapping patches along a simulation path by optimally cutting the patches so that they overlap with minimum discontinuity (Mahmud et al., 2014). But the drawback of these methods is they make conditioning difficult whereas DS honour conditioning data easily by assigning them to the closest grid node in the SG prior to simulation. In addition, DS can perform stochastic simulation using incomplete training images (TIs), even in multivariate case (Mariethoz & Renard, 2010).

Due to aforementioned reasons, DS is well-suited simulations technique for data reconstruction and several studies that successfully implemented DS for gap filling further strengthened the choice. Researches related to the application of the DS for reconstruction of gaps have been listed below:

1. Mariethoz et al. (2012) used DS to reconstruct spatiotemporal gaps in multivariate fields caused by clouds, atmospheric condition and satellite scan track error. The four variables (latent heat flux, surface temperature, soil moisture and shortwave downward radiation) with non-linear dependency with each other were used for reconstruction. The authors successfully reconstructed complex spatial patterns and fine-scale structure in gaps larger than the spatial structure. However, the authors used regional climate model (RCM) simulations as the synthetic proxy for remote sensing images.
2. DS algorithm was implemented by Oriani et al. (2014) for time series simulation of daily rainfall. Here, both the occurrence and the amount of the daily rainfall were simulated simultaneously. They were able to use incomplete TIs and show DS could successfully handle missing values in the TI.
3. Mariethoz et al. (2015) presented a method to repair gaps in multivariate time-series processing by matching patterns from training data to fill in missing data using DS. Linear as well as non-linear dependencies between the variables were maintained. Even though the method was presented applying geophysical signal processing, the authors claimed potential applications are in various environmental variables such as hydrology and meteorology.

4. Yin et al. (2015) demonstrated the reconstruction of the gaps in the Landsat ETM+ caused due to the failure of Scan Line Corrector applying DS method. The authors tested gap filling process in univariate case and bivariate case. In univariate case, the gapped image was filled using information coming either from non-gapped image of other date or from non-gapped region of the image itself. Reconstruction result using information from non-gapped area of the image was acceptable because only small portion of the image was unknown. In bivariate case, the gapped image was repaired by taking its own reflectance value as primary variable and reflectance of another image of same area acquired at different date as an auxiliary variable. The bivariate simulation provided more accurate reconstruction results because information between the images was complementary.

Apart from gap filling purposes MPS has been applied in other applications in RS domain and presented here for completeness:

1. Consensus-based fusion of spectral information from supervised maximum likelihood classification (MLC) and spatial structure information from MPS was used by Ge & Bai (2011) to extract roads and non-roads. Regardless of the proportion of the fusion of the MLC and MPS information, the authors found that classification accuracy of the combination of spatial and spectral information is greater than that of MLC. The increased accuracy was attributed to MPS being able to mimic complex connectivity pattern of roads from hand-drawn TI.
2. Tang et al. (2013) applied MPS simulation for post processing of land cover classification result of maximum likelihood classifier. An improvement of classification accuracy relative to post-processing based on traditional spatial filtering and the contextual Markov Random Field (MRF) classifier was obtained. These improvements were attributed to the increased classification accuracy for curvilinear classes whose spatial patterns cannot be modeled with variogram.

The study case here deals with the LOS displacement which is a continuous variable and the TIs to be employed are gapped displacement maps. As discussed above, DS can handle these situations with computational efficiency.

2.3. CONVENTIONAL GEOSTATISTICS FOR BENCHMARKING

Extensive literatures on conventional geostatistics are available. Therefore, they are not described here. For detailed explanation, the readers are referred to the books by Cressie (1993) and Journel & Huijbregts (2003). Discussions of geostatistics in context of remote sensing are provided by Addink (1999), Curran & Atkinson (1998), Van der Meer (2012) and Woodcock et al. (1988).

Geostatistical methods outperform the other deterministic methods like IDW and spline because these methods model the spatial dependence of the variables explicitly using the semivariogram (Addink, 1999; Curran & Atkinson, 1998). Kriging is a well-established geostatistical method. There are several kriging methods such as Ordinary Kriging (OK), Universal Kriging (UK), Indicator Kriging (IK), Co-kriging (CK) and others. OK assumes a stationary unknown mean while UK estimates a trend in data by simple functions and removes them before interpolation (Cressie, 1993).

In this study, OK has been selected for reconstructing the missing values in displacement map derived from DInSAR because the model used by OK to capture spatial dependence is simpler than that of UK. OK is the most commonly used kriging method (Kis, 2016; Malvic & Balic, 2009). Moreover, in previous studies carried out by the Yaseen et al. (2013) and Yaseen et al. (2013), the missing values in the InSAR derived LOS displacement map were interpolated using OK. For these reasons, OK has been used for benchmarking the results of MPS.

3. STUDY AREA AND MATERIALS

This chapter provides description of the study area, data and software used during the research. First of all, the study area, its local setting and reasons for selecting it are explained in section 3.1. Followed by the description of dataset selected and it's rationale in section 3.2. Lastly, details of software used are described in section 3.3.

3.1. STUDY AREA

Apart from Polar region, Himalaya is one of the widely glaciated areas in the globe. In recent years, these mountain glaciers are becoming vulnerable to climate change. It is becoming important to monitor these glaciers' response to the climate change.

The study area is Ngozumpa glacier, which is located at 28^0 00' N longitude and 86^0 45' E latitude. The glacier lies in Dudh Koshi basin and is 25 km west of the world's highest mountain, the Everest, in Nepal. Out of 664 glaciers in this region, Ngozumpa is the longest debris-covered glacier in the Himalayas (Higuchi et al., 2010). It is 18 km long and 1.2 km wide, with lower 15 km marked as ablation zone. The accumulation area of this glacier is situated on the upper slopes of the Cho Oyu, the world's sixth highest mountain (8188 m asl), and Gyachung Kang, the world's fifteenth highest peak (7922 m asl). The elevation at the terminus of Ngozumpa is 4680 m. It flows towards south-east. Gaunara glacier, a main tributaries following from the East, is no more connected to the Ngozumpa glacier (Benn et al., 2000).

It is shrinking, producing melt water, forming series of moraine-dammed lakes in the western side valleys and large supraglacial lakes on its low slope ablation zone. This is creating prominent threat of GLOFs to the downstream Sherpa villages (Thompson et al., 2012). This has ignited a lot of scientific interest in the area. Studying the glacier as such helps in anticipating possible future catastrophe, monitoring for early warning of potential catastrophes, mass balance studies and understand glacier dynamics. Several studies of this glacier have already been carried ~~out~~ and these studies would be valuable for comparison purposes (Quincey et al., 2009).

Figure 3.1 shows the study site in band combination used for glacier and snow mapping in the Sentinel-2 optical image (bands 11,8A, 3 as RGB), as used by (Egbers, 2016), where snow is seen in light blue, glacier in dark blue and debris-covered area and surrounding moraine in red.

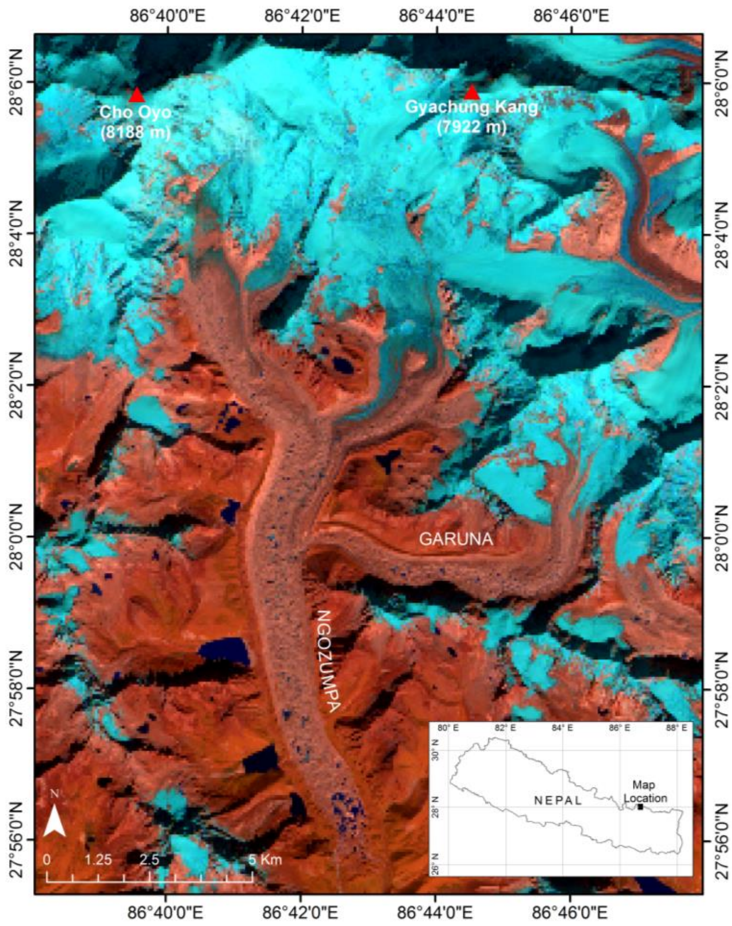

Figure 3.1: Location of Ngozumpa glacier, Nepal shown in Sentinel-2 false colour image (Level-1C bands 11, 8A, 3 as RGB) date 2016-10-30

3.2. DATA DESCRIPTION

For InSAR application, the coherence between the SAR image pair should be preserved. In glacier surfaces, precipitation, both in the form of snow and rain, and redistribution of snow by wind causes severe loss of coherence in entire area of glacier making InSAR inapplicable (Strozzi et al., 2002; Strozzi et al., 1999). To maximize the possibility of maintaining the coherence, SAR images with temporal baseline of 6 days (the least possible temporal baseline of S1) and of the coldest time of the year but with no precipitation were selected.

The Sentinel-1 images are captured in four modes, namely, Strip map (SM), Interferometric Wide Swath (IW), Extra Wide Swath (EW) and Wave (WV). The default pre-defined acquisition mode of Sentinel-1 over land is IW. The available images in the AOI are also in IW mode. Each mode produces four data products namely Level-0 Raw, Level-1 Single Look Complex (SLC), Level-1 Ground Range Detection (GRD) and Level-2 Ocean. Level-1 SLC products comprise of geo-referenced focused SAR data with preserved phase information, hence it is suitable for interferometric processing. Whereas level-1 GRD is processed further to make square pixel. This process is called multi-looking and it destroys the phase information so interferometry is no longer possible (ESA, 2013b).

Following pre-requisites for InSAR were checked before selecting the image pairs:

- Both images have to be acquired by the identical satellite using same acquisition mode and properties such as beam, polarization, off-nadir angle, etc.;
- Both images have to be captured with the satellite in the same nominal orbit;
- Baseline between the master image and the slave image should not be greater than the critical baseline. Further, the baseline should be as small as possible so that the topographic contribution in the interferometric phase is minimal. Additionally, the shorter baseline results in higher coherence.

ESA's archive was inspected to find out images suitable for InSAR application with short repeat pass delays (6 days). The images covering the chosen glacier applying the constraints explained above were downloaded from Alaska Satellite Facility. The downloaded images were level-1 SLC product.

The SAR images over AOI were acquired at dual polarization (VV and VH). For glacier velocity retrieval, the VV channel was used in this study over cross-polarized VH return because of its higher signal-to-noise ratio and less backscattering variation (Nagler et al., 2015). VV-VV polarization yields the highest coherence due to higher SNR ratio and less back-scattering variation (Papathanassiou & Cloude, 2014). Table 3.1 shows the details of the SAR image pairs used in this study:

Table 3.1: List of S1 SAR image pairs used for InSAR of the Ngozumpa glacier.

SAR Image Pairs	Master image	Slave image	Perpendicular Baseline (m)	Track	Temporal Baseline (days)	Polarization	Ascending /Descending Orbit
Pair I	2016-10-27 (S1-A)	2016-11-02 (S1-B)	+32.45	121	6	VV	Descending
Pair II	2016-11-02 (S1-B)	2016-11-08 (S1-A)	-42.13	121	6	VV	Descending

3.3. SOFTWARE DESCRIPTION

The following were the software used in the study:

1. **Sentinel Application Platform (SNAP) version 4.0.0**: SNAP4.0 is ESA's the joint architecture for Sentinel-1, -2 and -3 toolboxes that is available freely from http://step.esa.int/main/download/. Further development is still being carried out jointly by Brockmann Consult, Array Systems Computing and C-S (ESA, 2016). SNAP4.0.0 is the latest version used during this research.
2. **ArcGIS 10.3.1**: For pre-processing of the images such as image mosaicking, sub-setting the study area, and cartographic visualization purposes, the aforementioned software was used.
3. **R programming software**: R is free software for statistical computing and graphics(R Core Team, 2016). For format conversion (i.e. gslib to tif and vice versa) and the quantitative error analysis packages such as raster (Hijmans, 2016) and rgdal (Bivand et al., 2016) were used. For ordinary kriging, sp (Pebesma & Bivand, 2005) and gstat (Pebesma, 2004) packages were applied.
4. **DS: Multiple-Points Simulation by Direct Sampling (DeeSse):** It is DS executables written in C (Straubhaar, 2016). It is the core program implemented for MPS simulations.
5. **Stanford Geostatistical Modeling Software (SGeMS)**: It is open-source MPS software (Remy, 2005). This software was employed for visualizing and assessing MPS simulation results.

4. METHODS

The methods undertaken chronologically during the research are presented in this chapter. At first, section 4.1 explains in detail the processing chain of SAR interferometry from the starting—SLC SAR focused images to the final—surface displacement maps. Then, section 4.2 describes the OK implementation for interpolating the missing values in the displacement maps. Similarly, section 4.3 focuses on MPS application for reconstructing the gaps in the displacement maps. Finally, section 4.4 explains the accuracy assessment of the reconstruction results of both OK and MPS.

4.1. PROCEDURE OF SAR INTERFEROMETRY

The theory of SAR interferometry is given by (Fatland & Lingle, 1998). The adopted workflow of DInSAR to derive displacement has been shown in Figure 4.1 and each execution step has been discussed in detail below.

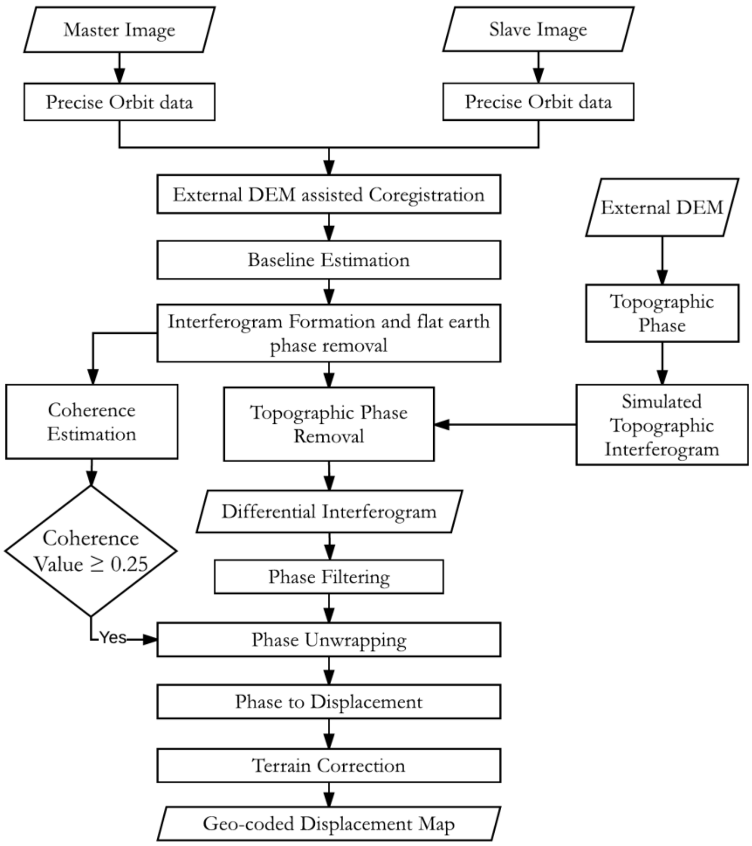

Figure 4.1: Adopted workflow of DInSAR to obtain glacier displacement map.

In order to compute the interferogram, first the image pair needs to be co-registered by moving the pixels in the slave image to align with the master image at sub-pixel accuracy. The image acquired at earlier date was used as the master, while the one with later acquisition date was taken as slave to get positive deformation in time.

Due to the TOPS mode of S1 IW data, higher co-registration accuracy is required. Geometric co-registration was performed using precise orbit data and SRTM 3-sec DEM. This process makes sure that each ground target contributes to the same pixel in both images (i.e. the master and the slave). The optional procedure to further refine the azimuth shifts is to use enhanced spectral diversity and incoherent cross correlation. These procedures are only applicable to TOPS mode interferometry in stationary areas and are not applied to glacier due to non-stationary scene. Further, these steps are not required because the S1 satellite tracking is highly accurate (Yague-Martinez et al., 2016).

During the co-registration, precise orbit files provided by the Precise Orbit Determination (POD) service for S1 were automatically downloaded by the SNAP Toolbox and applied for precise orbit correction. Precise orbit files are made available 20 days after the acquisition. The high geolocation accuracy of S1 with the precise orbit data enables precise co-registration of repeat-pass image pair without using ground control points (Nagler et al., 2015).

From the co-registered image pair, an interferogram was formed by the multiplication of master SAR image with the complex conjugate of the slave image. The resulting interferogram represents the phase difference between the two co-registered SAR image pair and is displayed as colour fringes. For C-band S1, each fringe (2π) in the interferogram corresponds to half the wavelength i.e. 2.8 cm displacement in LOS direction.

With repeat-pass interferometry, which is the case in this research, interferometric phase ($\Delta\varphi$) is affected by both the topography ($\Delta\varphi_{topo}$) and surface displacement towards or away from radar LOS direction ($\Delta\varphi_{disp}$). Apart from these two deterministic components, other contributors to the interferometric phase are atmospheric delay ($\Delta\varphi_{atm}$), flat earth phase ($\Delta\varphi_{flat}$) and other sources of noise ($\Delta\varphi_{noise}$). Thus, the interferometric phase equation given by Schneevoigt et al. (2012) is:

$$\Delta\varphi = \Delta\varphi_{flat} + \Delta\varphi_{topo} + \Delta\varphi_{disp} + \Delta\varphi_{atm} + \Delta\varphi_{noise} \tag{4.1}$$

In order to obtain $\Delta\varphi_{disp}$, the phase contribution from other sources should be eliminated.

Flat-Earth phase ($\Delta\varphi_{flat}$) is the phase attenuated in the interferometric signal due to the earth's curvature. The flat-Earth phase is estimated by means of the precise orbital and metadata information and deducted from the interferometric phase.

From the precise DEM, a synthetic interferogram containing only the topographic phase ($\Delta\varphi_{topo}$) was constructed. Then, the synthetic interferogram was subtracted from the real interferogram such that the resulting interferogram no longer contains topographic phase term (Joughin et al., 1996; Mattar et al., 1998). In this study, SRTM 3-sec DEM (90 m spatial resolution) was used to calculate the topographic component of the interferometric phase.

The error in the DEM causes inaccurate removal of topographic phase from the interferogram. But the LOS displacement measurement is robust to DEM error. For example: with a perpendicular baseline of 100 m, a 10 m error in DEM introduces error of only 0.1 cm/day in LOS direction (Joughin et al., 1996). Since the perpendicular baseline is shorter in this study (see Table 3.1); the interferometric phase is less sensitive to the reference DEM (Mattar et al., 1999). Thus, the use of SRTM 3-sec DEM is sufficient for this study.

In an ideal condition, $\Delta\varphi_{atm}$ is completely removed in the DInSAR process. However, due to changing water vapour content in atmosphere, $\Delta\varphi_{atm}$ may differ between repeat pass acquisitions. This is difficult to account for because the additional data needed should cover the entire atmospheric strata and is rarely available (Rott, 2009).

Finally, phase noise ($\Delta\varphi_{noise}$) was reduced applying Goldstein Filter (Goldstein & Werner, 1998) which is a non-linear adaptive filter. This process enhances phase unwrapping by improving the fringe visibility in the area with low coherence value. After removal of $\Delta\varphi_{noise}$, the resulting interferometric phase only comprises phase due to LOS displacement.

The InSAR coherence is defined as the complex cross-correlation coefficient of two complex SAR images. The coherence value ranges between 0 to 1, where 0 refers to fully decorrelated signals and 1 denotes perfectly correlated signals. The InSAR coherence is computed using Equation 4.2.

$$\rho = \frac{\left|\sum_{i=1}^{N}\sum_{j=1}^{M} C_1(i,j)\, C_2(i,j)^*\right|}{\sqrt{\sum_{i=1}^{N}\sum_{j=1}^{M} C_1(i,j)\, C_1(i,j)^*}\sqrt{\sum_{i=1}^{N}\sum_{j=1}^{M} C_2(i,j)\, C_2(i,j)^*}} \tag{4.2}$$

where C_1 is master complex image, C_2 is slave complex image, $C(i,j)$ is complex value at pixel location (i,j) where i and j denotes the range and azimuth direction respectively, x^* represents the complex conjugate of x, N and M are the number of pixels in range and azimuth direction respectively (Zhou et al., 2009). Coherence image was obtained from coregistered SAR image pair.

Phase unwrapping process of the interferogram is carried out to convert the 2π cyclic fringes into continuous signal using Minimal cost flow (MCF) technique with triangulated irregular network (TIN) (Costantini, 1998) or region growing technique (Baldi, 2003). During phase unwrapping, integer multiple of 2π is added to $\Delta\varphi$ whenever it jumps to 0 from 2π. As low coherence value cannot be unwrapped, Schneevoigt et al. (2012) suggested masking them out during phase unwrapping. The coherence value of 0.25 was taken as threshold and phases having coherence lower than the threshold were not considered for phase unwrapping (Bhattacharya et al., 2012; Wegmuller & Werner, 1997).

Phase unwrapping was carried out using 1 × 1 tile so that there is no vertical and horizontal linear jumps in the colour fringes from tiling in the unwrapped interferogram. MCF technique was applied here. The statistical-cost, network flow algorithm SNAPHU was used for phase unwrapping (Chen & Zebker, 2002).

Permanent markers such as rocks on the sides of the glacier were identified in the image. Since they have stable surfaces, they preserve the phase. Thus, the phase difference in the interferogram at these markers should always be zero. Atmospheric attenuation was removed from the interferogram by deducting the phase value at these markers (Zhou et al., 2009). The other purpose served by these permanent markers is for conversion of the relative surface displacement value to absolute. The displacement value obtained so far is relative. Reference point either with zero displacement or with known velocity should be identified in the interferogram to obtain absolute displacement value. Here, surrounding rock has been used as reference point with zero displacement (Berthier et al., 2005; Strozzi et al., 2007). The value of the chosen reference marker was subtracted from the relative displacement map. Finally, absolute displacement map was obtained.

The unwrapped interferogram was geocoded using SRTM DEM and Range-Doppler approach such that the map coordinates were projected to Universal Transverse Mercator (UTM) zone 45-north and World Geodetic Co-ordinate system 1984 (WGS-84) datum. In this way, geocoded displacement map was obtained.

4.2. ORDINARY KRIGING

4.2.1. Variogram analysis

Ordinary Kriging (OK) is a geostatistical method based on variogram (2γ) to determine the spatial dependence. It is often referred as a semivariogram (γ). They are exactly same except that semivariogram is half of the variogram. Equation 4.3 mathematically expresses a variogram (Isaaks & Srivastava, 1989).

$$2\gamma(h) = \frac{1}{m(h)} \sum_{i=1}^{m(h)} [z(u_i) - z(u_i + h)]^2 \tag{4.3}$$

where $m(h)$ is the number of data pairs at lag h, $z(u_i)$ is the value at location u_i and $z(u_i + h)$ is the value at location $(u_i + h)$.

First, an experimental variogram was calculated. Then, the experimental variogram was approximated by a best fitting theoretical model. Most commonly used theoretical models are Spherical, Exponential and Gaussian (Webster & Oliver, 2007).

$$\gamma(h) = \begin{cases} c_0 + c_1 \left[\frac{3h}{2a} - \frac{1}{2}\left(\frac{h}{a}\right)^3\right] & for\ h \leq a \\ c_0 + c_1 & for\ h > a \end{cases} \quad \text{Spherical model} \tag{4.4}$$

$$\gamma(h) = c_0 + c_1 \left[1 - exp\left(-\frac{h}{a}\right)\right] \quad \text{Exponential model} \tag{4.5}$$

$$\gamma(h) = c_0 + c_1 \left[1 - exp\left(-\frac{h^2}{a^2}\right)\right] \quad \text{Gaussian model} \tag{4.6}$$

where $\gamma(h)$ is a semivariance, h is lag, a is range, c_0 is nugget variance and $c_0 + c_1$ is sill.

4.2.2. Ordinary Kriging interpolation

OK is used to predict the missing displacement values at a selected location u_0 from a linear combination of surrounding known displacement values at locations u_i. A relevant weighting coefficient (λ_i) is assigned to each selected surrounding locations which determines the influence of each known data on the final estimation at the selected grid node. The weighting coefficient (λ_i) sum to 1. The relationship between the existing sample data and the estimation point is established by the modelled variogram, or by covariance (matrix) in case of second order stationarity. OK equation is written as (Malvic & Balic, 2009):

$$\hat{z}(u_0) = \sum_{i=1}^{n} \lambda_i z(u_i) \tag{4.7}$$

4.3. DIRECT SAMPLING

The implementation of the DS algorithm used in this research is called DeeSse (Straubhaar, 2016). The basic principle of DS method is to use TI to identify spatial features and properties which can be used to fill the gaps. The missing values of the LOS displacement map are sequentially replaced by matching the patterns of the TI with the values of the neighbouring pixels. Hereafter, the glacier displacement image with gaps to be reconstructed is addressed as the target image, while the image providing information for filling gaps in target image is referred to as the input image.

Let $Z(x)$ be the variable of interest to be simulated, where the gapped pixel in the target image is denoted by x. Similarly, N_x is the ensemble of the n closest pixels of x that are informed. These n pixels define the neighbourhood. The concept of DS method is to find one possible outcome of Z conditional to N_x from the conditional cumulative function given in Equation 4.8:

$$F(z) = \text{Prob}(Z(x) \leq z | N_x) \quad (4.8)$$

The basic idea is to find another pixel y in the TI (in this study case input image) that has neighbouring pixels N_y similar to N_x. The distance $d(N_x, N_y)$ is used to compare the similarity between N_x and N_y. The concept of distance is flexible and can be applied to both categorical and continuous variables. There are several possible methods to compute distance $d(N_x, N_y)$, depending on the type of the variable to be reconstructed. For detailed discussion on the different proposed distances for both categorical and continuous variable, Mariethoz et al. (2010) and Mariethoz & Kelly (2011) can be referred.

Since the variable of concern in this research is continuous, the distance adopted was the Weighted Euclidean distance, as suggested by Mariethoz et al. (2012) to be used for continuous variable. The Equation 4.9 is used to compute the distance.

$$d(N_x, N_y) = \frac{1}{\eta}\sqrt{\sum_{i=1}^{n} w_i \ [Z(x_i) - Z(y_i)]^2} \quad (4.9)$$

where w is weight of each node and η is normalization factor applied so that the value of distance is bounded in the interval [0, 1]. It is the maximum difference between the two values of Z in the TI.

Apart from the Weighted Euclidean distance, normalized pair wise Manhattan distance can also be adopted for continuous variable and can yield comparable results. Even though the results of both Manhattan and Euclidean distances are very similar, Weighted Euclidean distance was chosen because it is straight-line distance and is invariant to the rotation of the co-ordinate system.

The path followed in search for y in the TI can be random or unilateral. In this study, random search path has been used.

In case of continuous variable, the perfect match between the data events in the TI and SG is often not found which is why an acceptable threshold t is introduced. During the scanning process of TI, when the pixel y is found in the TI with the distance smaller than predefined threshold t, the value $Z(y)$ is picked and assigned to $Z(x)$. If the search area has reached a predefined maximum search fraction f of the TI but unable to find a pixel y satisfying the threshold requirement, then the pixel y with the lowest distance is accepted and its value $Z(y)$ is assigned to $Z(x)$.

Figure 4.2 graphically illustrates the DS process. The data event is defined in Figure 4.2 (a) and the central pixel with a question mark represents the target pixel to be filled, and the black and the two white pixels are neighbourhood with known values from either previous simulation or are conditioning data assigned to SG prior to the simulation. Here, a categorical case where a pixel can take only two values—0 (white) and 1 (black) is dealt with. Figure 4.2 (b) shows how the search window is defined in the TI grid by using the dimensions a, b, c, d of the data events from Figure 4.2 (a). Figure 4.2 (c) shows carrying out search in the search window of TI using data events. The search moves to next location following random path until the simulation data event is matched satisfactorily as shown in Figure 4.2 (d). Then the value of the central pixel of the first matching data event is assigned to the target pixel Figure 4.2 (e). In this case, the data event in the TI and the data event in the SG match exactly hence the distance is zero and the value $Z(y)$ =1 is assigned to the SG.

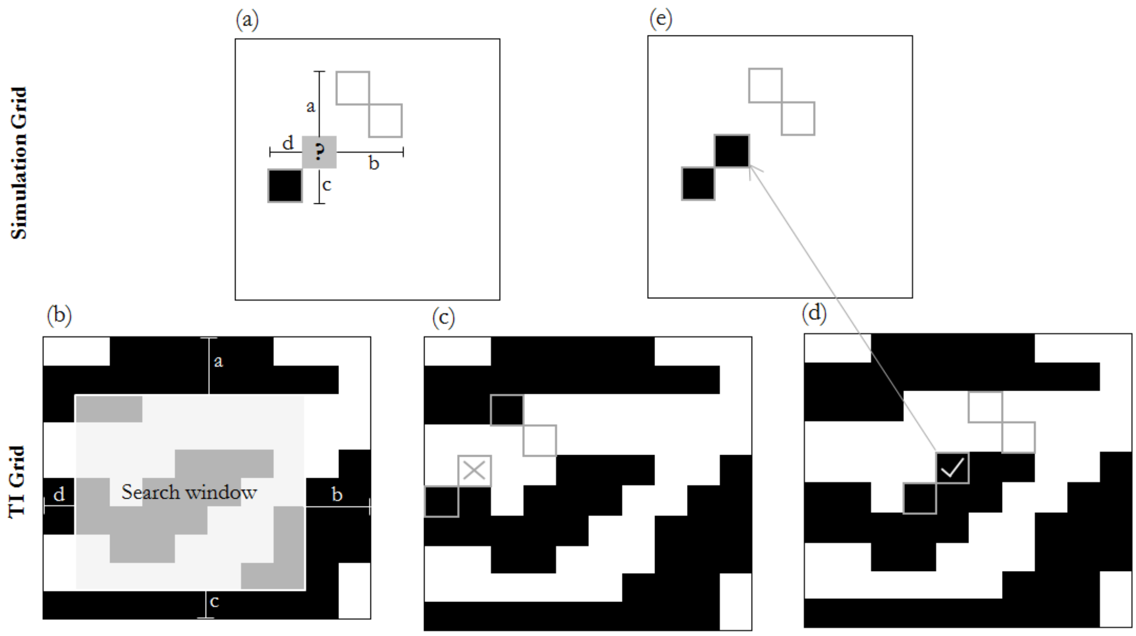

Figure 4.2: Graphical illustration of DS method. (a) Define the data event in the target image. (b) Define a search window in the TI grid. (c) Scan the TI using the search window until (d) the simulation data event is matched satisfactorily. (e) Assign the value of the central pixel of the first matching data event to the target pixel (Mariethoz et al., 2010).

The DS method is easily extended to the multivariate case. The distance between multivariate neighbourhoods is computed by a weighted average of the distances taken individually for each univariate neighbourhood. Equation 4.10 gives the distance equation for multivariate case.

$$d\left(N'_x, N'_y\right) = \sum_{j=1}^{m} \frac{\alpha_j}{\eta_j} \sqrt{\sum_{i=1}^{n} w_i^k \; [Z^k(x_i) - Z^k(y_i)]^2} \qquad (4.10)$$

where m is the number of variable, α_j and η_j are the weights and the normalization constant for each variable respectively.

4.3.1. Construction of the Training Images

Since MPS simulations strongly rely on TIs, choosing appropriate TIs is of first priority as is semi-variogram modelling in traditional two-point geostatistics (Boisvert et al., 2007). Choosing appropriate TIs is not straightforward. There are several ways to construct TIs. For example, TIs can be drawn by hand then numerically represented by digitization (Ge & Bai, 2011; Strebelle & Remy, 2005). They can also come from remote sensing images and remotely sensed classification results (Tang et al., 2013). Both custom build TIs that suites the application or TIs from TIs database that have been built for the application of interest can be applied. However, in this particular study case the latter is not available yet, which is why TIs were specifically custom made taking into account the application in hand.

Since TIs should contain the variability, connectivity and structural properties of the phenomenon under investigation and DS can perform simulations using incomplete TIs, the LOS displacement maps generated from the SAR interferometry with the no data values in masked out incoherent area were used as the TIs.

The DS implementation is in the ANSI C language. All the input and output files are in an ASCII SGeMS compatible format (Remy et al., 2009). TIs should be numerically represented in a format such that they are compatible with the software being used. Since SGeMS is the applied software, TIs have to be in either in the sgems binary format or in the geostatistical software library (GSLIB) format. The LOS displacement maps were in .tif file format. The 2D images can be converted to GSLIB (.txt) format using open source software called TiConverter developed by Fadlelmula et al. (2016). Using the software in case of continuous variable requires picking up every possible value iteratively which is impractical. Thus, R codes were developed and used to convert the .tif to .gslib format (Appendix A. 1). R codes made the conversion process easy and practical as numerous files were to be converted.

The output files format generated from the DS were also in .gslib so R codes were made to convert them back to .tif file format.

4.3.2. Mask Image

Since the SG is defined by the number of nodes in x- and y-direction, the extent of SG is either rectangular or square. But the AOI for simulation is the irregular shape of the glacier. Mask image is supplied to the SG to flag the nodes either to be simulated or not. Mask image was constructed and applied on the SG such that the nodes outside the glacier extent were flagged not to be simulated. This constraints only the nodes corresponding to the glacier regime to be simulated.

4.3.3. Parameters of DS

Table 4.1 illustrates the value of the fixed parameters used and the range of values of the parameters varied for optimization in the DS algorithm.

Table 4.1: The fixed and varied DS parameters.

Fixed parameters		
Name		**Default**
Simulation Method		MPS
Number of realizations		10
Maximum Search Distance		690 488 0 (1/2 size simulation grid)
Path Type		0 (random path)
Type of variable		1 for continuous
Initial Seed		444
Parameter Reduction		1 (no parameter reduction)
Data conditioning		Yes
Weight of conditioning data (δ)		5
Distance Type		2 (Weighted Euclidean distance)
Post-processing		0 (No post-processing)
Varied parameters		
Name	**Default**	**Range**
Distance Threshold (t)	0.05	0.005 - 0.01 - 0.03 - 0.05 - 0.1 - 0.15 - 0.2
Maximum scan fraction of TI (f)	0.5	0.2 - 0.3 - 0.4 - 0.5 - 0.6 - 0.75 - 1
Maximum number of points in neighbourhood (n)	30	1 - 5 - 10 - 15 - 20 - 25 - 30 - 35 - 40

4.3.3.1. Maximum Search Distance

The neighbourhood N_x is defined as the n informed grid nodes that are closest to x within the defined search area. The search area is defined by the parameters of maximum search distance, which are the radii in the 3 x-, y- and z- directions of a rectangular search area. Normally, it is advised to set the radii to half of the SG to ensure the use of a large search area, corresponding to the maximum neighbourhood size (Mariethoz et al., 2010; Meerschman et al., 2013). Since the size of the SG in this study is (1379, 975, 0), maximum search distance is set to (690, 488, 0). Due to this, neighbourhood covering large portion of the search area is defined when the first unknown grid nodes are simulated. As the number of simulated nodes increases, gradually the size of the area covered by the N_x decreases. This process ensures that structures of all sizes are captured from the TI and presented in the simulation.

4.3.3.2. Conditioning data and weight factor for conditioning data

In DS algorithm, to honour the conditioning data, they are assigned to the closest grid node in the SG before the simulation starts. This assures the local accuracy because the grid nodes at the conditioning data locations will have the correct values. The non-gapped portions of the LOS displacement map were used as the conditioning data.

It is important that these fixed grid nodes are included in the spatial pattern or else they will appear as noise. Weight factor for conditioning data (δ) is parameter used to enforce the consistency of the pattern in the neighbourhood of the conditioning data. During the distance computation between the data events, δ is used to weight data event nodes that correspond to conditioning data. Meaning, if a value is a conditioning data, its corresponding contribution is multiplied by δ. When δ is 1, all the nodes are given the same weight during distance computation. If δ>1, the data event nodes corresponding to conditioning data are given higher weights. Conversely, if δ<1, they are provided lower weights. Thus, δ is an important parameter when conditioning data are available.

For δ =0, the simulation is unconditional because the conditioning data are ignored in distance computation between the data events. Thus, simulations show patterns inconsistent with the conditioning data. When δ=1, the simulation patterns are approximately consistent with the conditioning data, while increasing δ to 5, the simulation patterns are closely consistent with the conditioning data. It is advised to set the value of δ≥1 for honouring the conditioning data. If the expected uncertainty of the conditioning data is lower i.e. conditioning data is of high quality with no measurement errors, the higher δ can be used.

Since the conditioning data in this study are the displacement values generated from InSAR which can be considered to have minimum uncertainty, δ=5 has been used meaning the conditioning data weigh five times more than the already simulated grid nodes.

4.3.3.3. Post processing for noise removal

Post-processing option in DS is applied to further enhance the simulation quality through noise removal.

In the post-processing step, each node is resimulated using completely informed neighbourhood obtained from previous simulation. There are two post-processing parameters—the number of post-processing steps (p) and the post-processing factor (p_f). Second parameter, p_f, is the factor used to divide f and n to reduce additional computational cost in the post-processing (Mariethoz, 2009). For example, when p=3 and p_f=2 are assigned for post-processing, all the nodes are resimulated thrice using values of parameters f and n half of their original values.

In categorical case, post-processing option results in significant improvement of simulation with noise removed entirely for intermediate t values such as 0.1 and 0.2. But in continuous case, the post-processing step is unable to improve the simulation quality considerably and the CPU cost is very high (Meerschman et al., 2013). The quality loss caused by a high t in continuous case cannot be regained by applying one or more post-processing steps. Further, in both categorical and continuous cases, when small t is used, occurrence of noises in simulation is less thus improvement of simulation quality by post-processing is not-significant. Due to these reasons, post-processing step has not been applied in this study.

4.3.3.4. Varied parameters

The most important user defined parameters of the DS algorithm are (i) the number of neighbour (n), (ii) the distance threshold value (t) and (iii) the scan fraction of TI (f). To understand and access their impact in the simulation process and results, and the CPU cost, further analysis was conducted.

The use of the larger n, the smaller t and f closer to 1, results in better simulations. However, this might cause computational burden. The rule of thumb derived by Meerschman et al. (2013) for continuous TI was to use t≤0.1 and n≥30. Considering this, the parameters were varied as shown in the Table 4.1.

If ten unconditional simulations are performed for each parameter combination of 7 t values, 7 f values and 9 n values shown in Table 4.1, it would result in 4410 realizations for each DS case. There are three DS cases presented in this research (2 univariate and 1 bivariate). Full parameter selection would require rigorous search in all dimensions of the 3D parameter space defined by t, f and n. This will require tremendously large amount of time. Further, generating simulations based on the continuous TI such as displacement field takes longer (Meerschman et al., 2013). So instead, linear search approach was adopted for each parameter keeping the rest two constant. Only 1 realization was considered for parameter optimization.

4.3.4. DS cases

Two different DS cases were considered during the reconstruction process:

DS Univariate Case (DS_u): No separate TI was employed; the non-gapped area of the target image itself was used to reconstruct the gapped regions. When large portion of the target image is informed, non-gapped regions of the target image consists of sufficient information for filling gaps and can be used instead of external training image (Yin et al., 2015). Two displacement maps obtained for pair I and pair II were separately reconstructed in univariate fashion. The known displacement values obtained from each pair served as TI to fill in missing values in displacement map obtained from the same pair.

DS Bivariate Case (DS_b): Bivariate simulation, taking two displacement images together. In the bivariate situation, both the variables (i.e. displacement maps) to be simulated are partially known. The relationship between the variables was established through the TIs instead of expressing in terms of mathematical relation. DS co-simulates to reconstruct the gaps in both displacement maps obtained from pair I and pair II. To provide equal importance to both gapped displacement maps, identical values of 0.5 for the weights associated with each displacement map was used.

4.4. ACCURACY ASSESSMENT

To evaluate the performance of OK and DS, artificial gaps were created at locations with known LOS displacement values. For evaluating the results of the filled gaps in the target image, both qualitative and quantitative measures were employed.

For validation purposes, the known displacement values prior to the imposition of the artificial gaps were used as reference dataset. The values predicted using OK and DS at those artificial gaps were used as the measured dataset. From a quantitative perspective, Root Mean Square Error (RMSE) was employed as it is widely used performance validation measure in similar simulation studies. The difference between the measured/observed displacement value and the predicted displacement value is error (e). The Root Mean

Square Error $\left(\mathrm{RMSE} = \sqrt{\frac{\sum e_i^2}{n}}\right)$ was computed. However, RMSE alone is not an appropriate accuracy assessment metric due to its sensitivity to occasional large error. Additional measures namely histograms of simulation errors (e), scatterplots of the reference displacement values versus the simulated displacement values in the artificial gaps and the residuals distribution map (the mean of simulation results minus the original values before gap imposition) were applied to evaluate the reconstruction results.

To qualitatively assess the reconstruction results, visual inspection of existence of artifacts was carried out.

5. RESULTS

This chapter presents the results of DInSAR and reconstruction results of missing values in DInSAR derived displacement maps from OK and DS. Similarly, the outcomes of the comparative assessment of OK and DS reconstructions are presented in detail.

5.1. DINSAR

The procedures discussed in section 4.1 were applied for interferometric processing to create the interferograms. The interferograms of Ngozumpa glacier, before unwrapping, computed from SAR image pair I and II are shown in Figures 5.1(a) and 5.1(b) respectively.

Each fringe in the interferogram represents LOS displacement of 2.8 cm. The fringes of the interferogram are denser in the upper section of the glacier compared to the lower section, relating to the larger gradient of displacement in the higher elevated areas. The fringe pattern disappears gradually while moving towards the lower sections indicating that the Ngozumpa glacier is stagnant across its long debris-covered tongue.

Figures 5.1(c) and 5.1(d) illustrate the coherence images of the SAR image pair I and II. Taking a close look at the coherence images, it is observed that the coherence of the interferogram is high in the terminus and middle section of the glacier while the coherence gradually decreases as we move further towards the upper region of the glacier. The areas where the phase noise is high are the snow covered mountainous area in the upper part of the glacier. High coherence is observed in rocks/mountains next to the glacier where almost no snow or ice is present.

Comparing the coherence images in Figures 5.1(c) and 5.1(d) to their corresponding interferograms in Figures 5.1(a) and 5.1(b), it can be seen that the areas with fringes in the interferogram correspond to areas with high coherence in the coherence images. Similarly, the noise in the interferograms corresponds with areas with low coherence in the coherence images.

The two interferograms, shown in Figures 5.1(a) and 5.1(b), are almost identical; the fringe patterns are similar, having same size and location in both interferograms. This indicates that the displacement is approximately same in both interferograms.

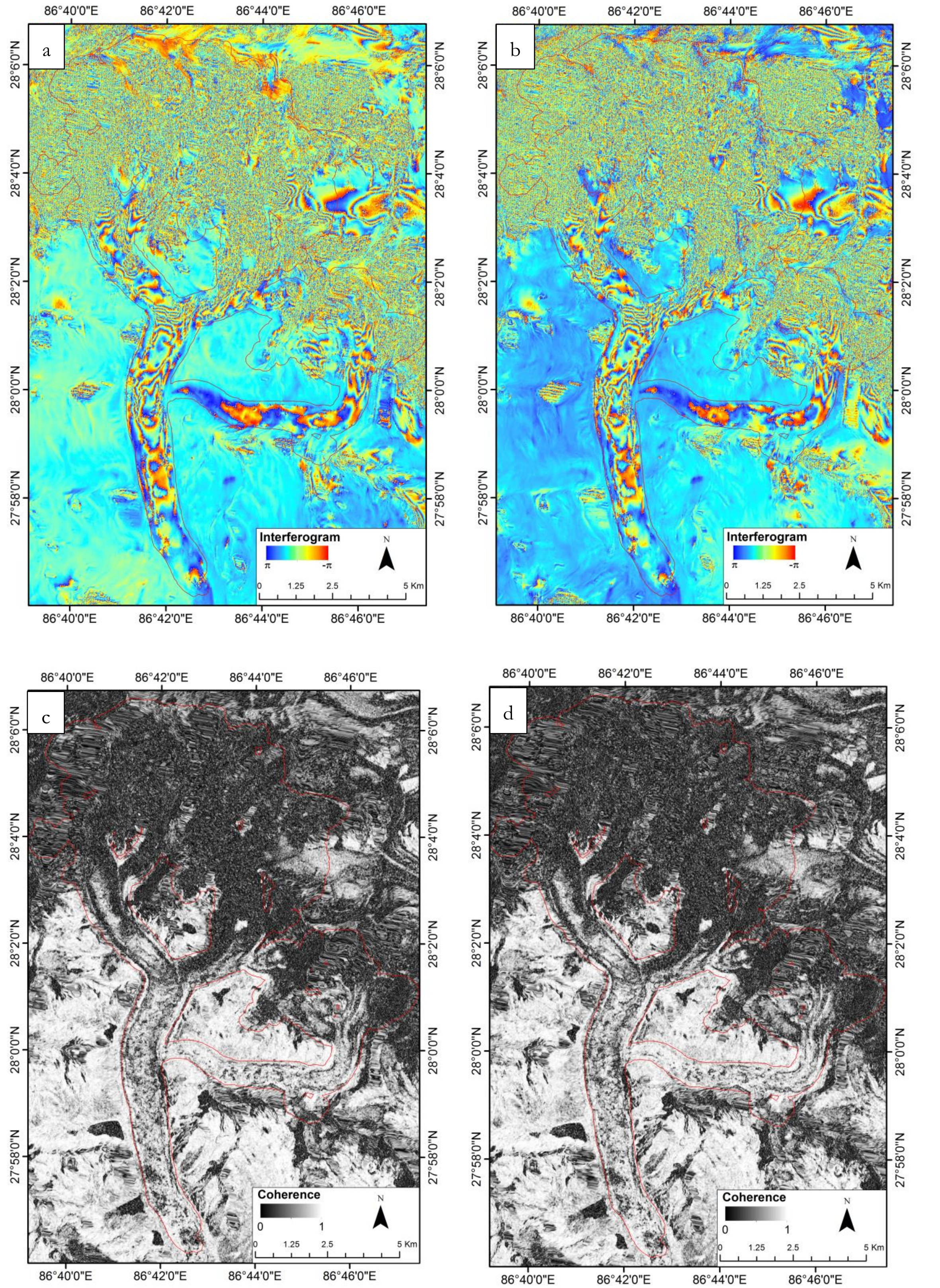

Figure 5.1: Results from DInSAR; Sentinel-1 SAR descending wrapped interferogram presenting LOS surface displacement of Ngozumpa Glacier due to ice motion during 6 days (a) between SAR image pair I (27-10-2016 to 02-11-2016); (b) between SAR image pair II (02-11-2016 to 08-11-2016). (c) The coherence image between the SAR image pair I. (d) The coherence image between the SAR image pair II.

The interferograms shown in Figures 5.1(a) and 5.1(b), after being unwrapped and geocoded, produced the glacier displacement maps as seen in Figures 5.2(a) and 5.2(b). Since the time interval between two consecutive images used to generate interferogram is 6 days, the displacement during this time interval can be measured and is shown in displacement maps. The positive values in the displacement map means the displacement is towards the radar's LOS direction whereas the negative values refers the movement is away from the radar's LOS direction.

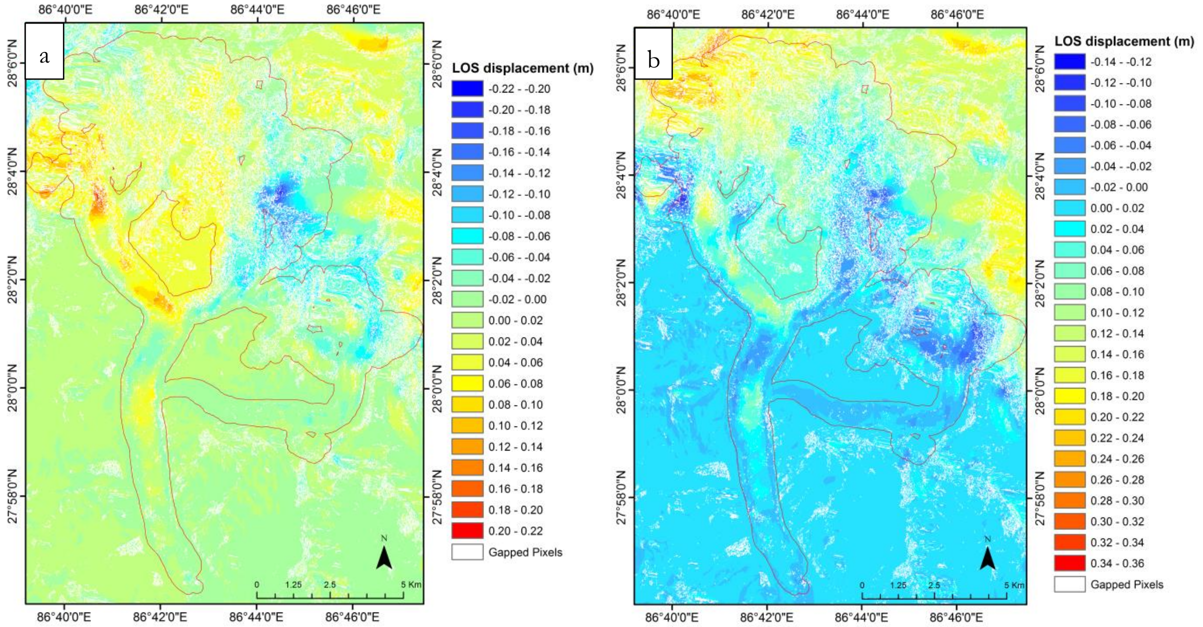

Figure 5.2: Ngozumpa glacier displacement (m) (a) from SAR image pair I; (b) from SAR image pair II. Missing values are shown in white. The displacement measurements are classified into classes with equal class interval of 0.02 m.

Visually comparing the coherence images with the S2 optical image in Figure 3.1, loss of coherence can be observed in the regions on the glacier covered by snow/ice (blue coloured part of the glacier in Figure 3.1). As a result phase noise is high in the interferogram and larger gaps are present at these locations in the displacement maps (see Figures 5.2(a) and 5.2(b)).

High coherence can be seen in debris-covered part of the Ngozumpa glacier (red coloured part of the glacier in Figure 3.1) and clear fringes can be observed in the interferograms. Consequently, the gaps in the displacement maps (see Figures 5.2(a) and 5.2(b)) at the debris-covered tongue of the glacier are few and small in size. This phenomenon can be explained by relatively lower displacement gradient and absence of snow/ice melt in the debris-covered part of the glacier.

5.2. DESCRIPTION OF THE ACTUAL GAPS IN THE GLACIER DISPLACEMENT MAP

The glacial displacement maps contained missing values. Altogether, there were 11066 and 11064 polygons of missing values in the displacement maps derived from SAR image pair I and pair II respectively and the details of those polygons are in Table 5.1.

The location of the missing displacement values in displacement maps from pair I and pair II can be seen in Figures 5.2(a) and 5.2(b) respectively. The gaps are of different sizes and some are large (thousands of pixels). The large gaps occur in the upper region of the glacier.

Table 5.1: Statistics of the gaps caused by low coherence in displacement map from SAR image pair I and pair II.

No. of pixels	Pair I		Pair II	
	No. of polygons	Area (m^2)	No. of polygons	Area (m^2)
1-14	9770	5476020	9820	5544911
15-34	706	3024994	645	2718591
35-84	349	3750797	358	3719767
85-149	120	2569684	127	2820465
150-965	117	6988517	108	6586876
966-2365	4	234095	6	1765230
	11066	**22044107**	**11064**	**23155840**

5.3. FORMATION AND DESCRIPTION OF ARTIFICIAL GAPS

Artificial gaps were created for the validation purposes. The gaps that occurred in the displacement maps due to loss of coherence were of different sizes and shapes. Small gaps can be repaired easily with high quality because the surrounding data provide sufficient information. Bigger gaps with different shapes and sizes were picked. They were shifted to non-gapped area and artificial gaps were made. They were treated as if they are unknown, and were consequently reconstructed and analysed.

The size of the gaps caused by the loss of coherence ranged from 1 to 1341 pixels for displacement map from pair I and from 1 to 2365 pixels for displacement map from pair II. In displacement map from pair II, there was a big jump from second largest gap with size of 1084 to the largest gap. The mean gap size was picked for the analysis because most of the occurring gaps were of or around this size and also the gaps should not be small as mentioned earlier. To reduce the influence of the outlier, polygon of size 2365 was ignored during the calculation of the mean gap size.

For evaluating the performance of the OK and DS, artificial gaps were imposed at 12 locations with the known glacial displacement values. To construct the 12 artificial gaps, a polygon consisting of 142 pixels was selected (approximately 27713 m^2 in area) from pair II. For simplicity, the same polygon was used to create artificial gaps at same 12 locations in both displacement maps from pair I and pair II. The interpolations were performed at those gaps. The predicted values were compared with the original values at each of the artificial gaps and RMSE was computed. These gaps are addressed as 12 shifted polygons in the following sections.

The location of the 12 shifted polygons in the displacement maps from pair I and pair II is shown in Figures 5.3(a) and 5.3(b) respectively.

To assess the impact of the big gaps sizes, additional two large polygons were chosen and artificial gaps were created by repositioning them at the same location. The reconstruction was performed one polygon at a time. DInSAR results showed that the westerly tributary of Ngozumpa glacier is active. It is a key location with comparatively heterogeneous displacement values. So the large gaps were imposed in the active part of the western tributary in the displacement map from pair II. Only DS_u simulation was performed. A polygon with 499 pixels was selected to impose intermediate gap. A polygon consisting 1016 pixels was chosen to create large gap because it was one of the largest occurring gap with the high number of the missing values. Figure 5.4 shows the location of the three shifted polygons of increasing sizes on the displacement map from pair II.

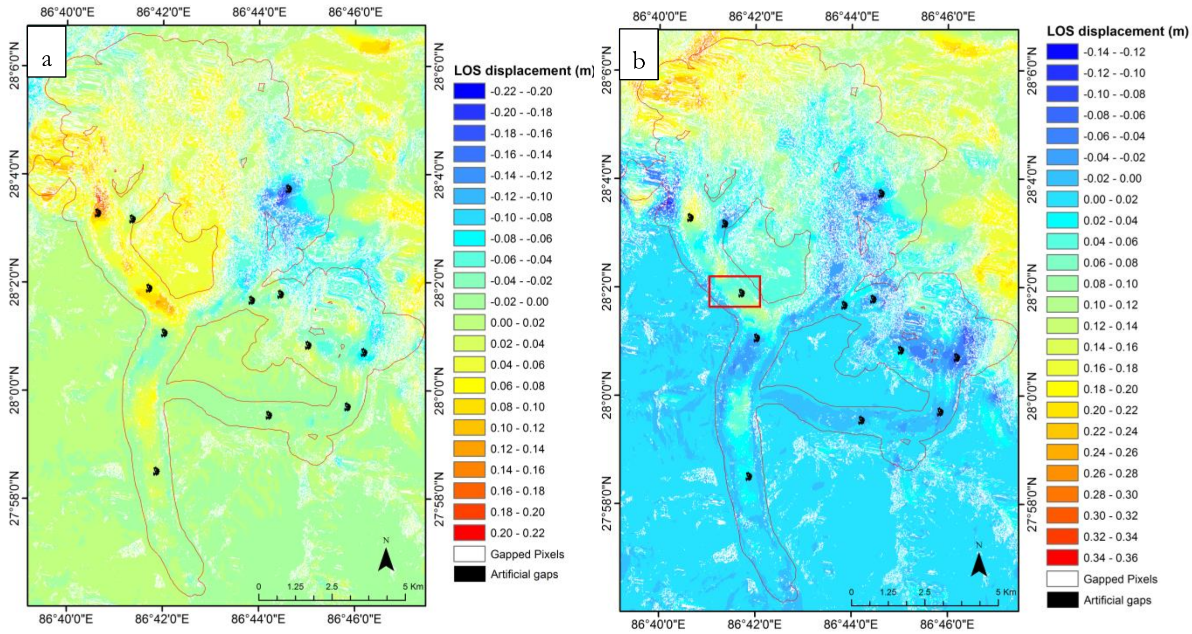

Figure 5.3: Twelve shifted polygons on the displacement maps from (a) pair I and (b) pair II. The actual gaps are in white and the 12 artificial gaps imposed are shown in black.

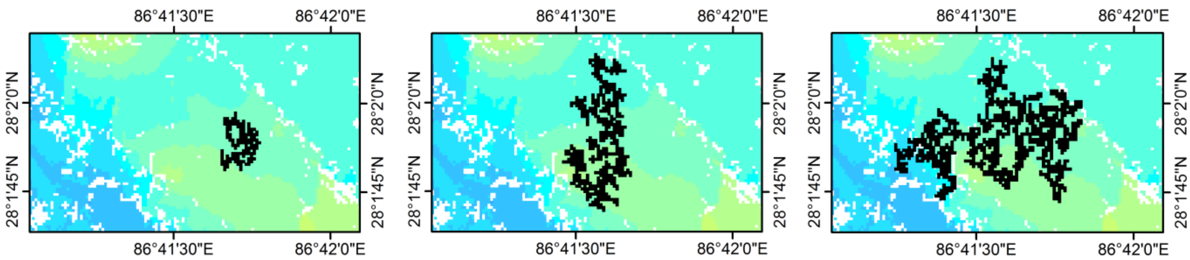

Figure 5.4: The polygons of increasing size imposed in key location of displacement map from pair II (shown in red box in Figure 5.3 (b)) for accuracy assessment of growing gap size. Artificial gaps imposed are: polygon 1 (142 pixels), Polygon 2 (499 pixels) and Polygon 3 (1016 pixels) from left to right respectively shown in black.

5.4. TWELVE SHIFTED POLYGONS

5.4.1. Ordinary Kriging

The 12 shifted polygons comprises of 1704 pixels. These were used for validation purposes. For OK, literature suggests maintaining the ratio of 1:3 for validation and calibration samples (Hamm et al., 2015). Thus, the 5100 samples (three times the number of artificially created gapped pixels) were drawn randomly from the known parts of the displacement map. Further, the distribution of the samples in the study area was assessed. They were evenly distributed across the area of interest.

Exploratory data analysis performed prior to variogram analysis showed that the distribution of samples data for pair I and pair II are sufficiently normal (see Figure 5.5). Some evidence of skew in the pair II was seen, but this can be neglected. So, variogram analysis was continued with the untransformed data.

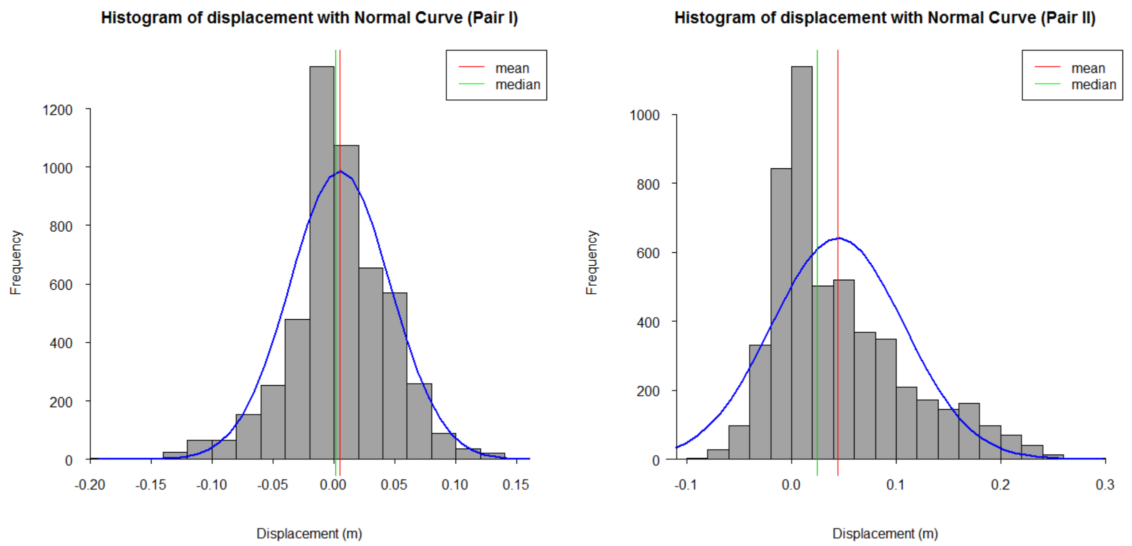

Figure 5.5: Histograms of sample points for displacements from pair I and pair II with fitted normal curve (blue).

The parameters of variograms for displacement variable from both pair I and pair II are given in Table 5.2. Figure 5.6 graphically shows the experimental variogram and fitted Exponential theoretical model for displacements from pair I and pair II. For pair I, experimental variogram was estimated using cutoff value 8000 and bin width 450 while for pair II, cutoff value 8000 and bin width 500 were used. The spatial dependency of the displacement values of both pairs was modelled by Exponential theoretical model. Exponential model best fitted the both experimental variograms with the least sum of square error (SSE). The small nugget value approaching zero for both fitted variograms indicates variability is highly correlated in space.

The actual and artificially imposed missing values in the displacement maps shown in Figure 5.3 were interpolated using OK. The validation results of the OK interpolated values are provided in Table 5.6.

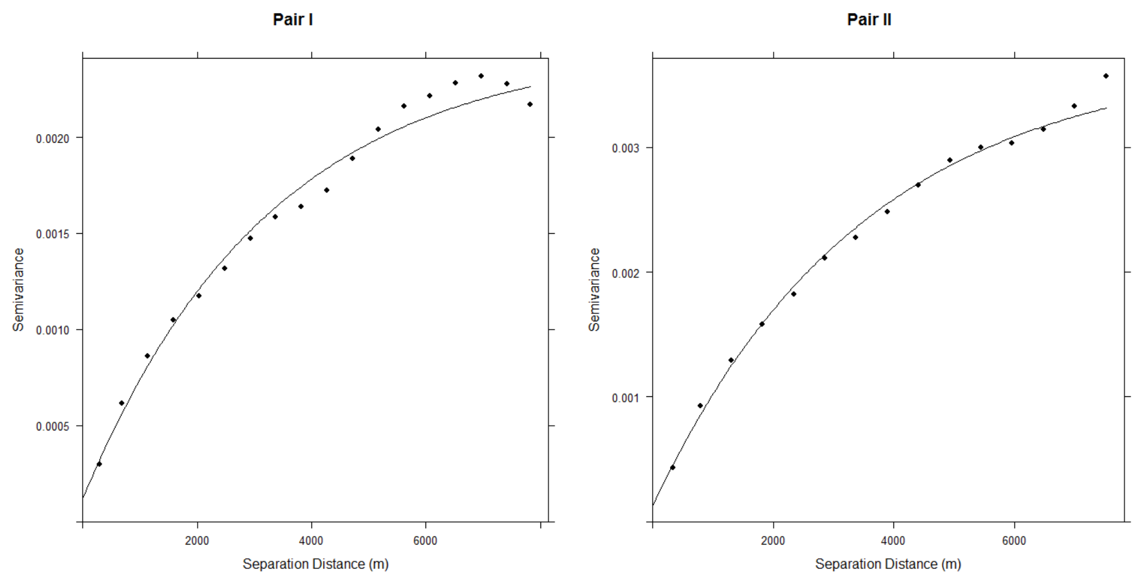

Figure 5.6: Fitted variogram (OK) for pair I and pair II. Variogram names and their parameters are shown in Table 5.2.

Table 5.2: Variograms for OK of displacements from image pair I and pair II. The fitted variograms are shown graphically is Figure 5.6.

Displacement map	Fitted Variogram				
	Model	Range	Sill	Nugget	SSE
Pair I	Exponential	3213.69	$2.48\text{x}10^{-3}$	1.18×10^{-4}	4.40×10^{-9}
Pair II	Exponential	3567.60	$3.78\text{x}10^{-3}$	1.28×10^{-4}	5.14×10^{-9}

5.4.2. Direct Sampling

First, the experimentation for both DS_u and DS_b cases were performed to decide the optimal parameters. The values of the fixed and the varied DS parameters used for experimentation are provided in Table 4.1.

For DS_u case, the results of the sensitivity analysis of three user defined parameters t, f and n are given in Table 5.3. As seen in the table, for pair I, n=15 resulted in the lowest RMSE value. For pair II, the optimal value of n is 10. Even though using value of n equals 30 results in slight improvement over n=10 (lower RMSE by 0.00005 m), the computational burden exponentially increased (over 10 times). Thus, to balance the computational cost as well as the simulation accuracy, n =10 was chosen. Regarding t, the simulation quality improved with decrease in t for both pairs but the CPU time grew exponentially. The t of 0.005 provided the least RMSE for both pairs. The improvement from t 0.01 to t 0.005 was very small (0.0005 m). So further decrease in t would result in insignificant improvement while the computational burden would increase by huge amount. Thus, the value of t lower than 0.005 was not further experimented. The value of t equals 0.005 was selected for both pairs. Similarly, simulation accuracy saturated at the value of f equals 0.3 for both pairs. The RMSE remained unchanged even increasing f to the maximum possible value of 1 but the computation cost increased. This clearly shows that f = 0.3 is optimal both in terms of accuracy and CPU time.

Table 5.3: DS_u parameter experimentation for displacement maps from pair I and pair II.

Distance threshold (t)	Pair I		Pair II	
	Time taken for simulation (S)	RMSE (m)	Time taken for simulation (S)	RMSE (m)
0.2	6	0.04720	15	0.04764
0.15	7	0.03714	23	0.03752
0.1	24	0.02507	36	0.02452
0.05	230	0.01374	549	0.01303
0.03	3088	0.00861	4620	0.00815
0.01	24934	0.00480	19813	0.00323
0.005	24985	0.00439	23048	0.00262
Maximum Scan Fraction (f)	Pair I		Pair II	
	Time taken for simulation (S)	RMSE (m)	Time taken for simulation (S)	RMSE (m)
0.2	189	0.01383	338	0.01366
0.3	239	0.01374	370	0.01303
0.4	248	0.01374	597	0.01303
0.5	270	0.01374	675	0.01303
0.6	272	0.01374	632	0.01303
0.75	282	0.01374	684	0.01303
1.0	460	0.01374	714	0.01303
Number of nodes (n)	Pair I		Pair II	
	Time taken for simulation (S)	RMSE (m)	Time taken for simulation (S)	RMSE (m)
1	3	0.02021	21	0.02045
5	19	0.01372	46	0.01398
10	43	0.01344	111	0.01308
15	91	0.01312	233	0.01313
20	142	0.01337	389	0.01327
25	192	0.01363	297	0.01311
30	274	0.01374	772	0.01303
35	367	0.01384	920	0.01306
40	480	0.01358	1214	0.01305

For DS_b case, the experimentation results of the three user defined parameters$t$, f and n are illustrated in Table 5.4. The DS_b results are same to that of DS_u case. The optimal values of n for pair I and pair II are 15 and 10 respectively as they resulted in least RMSE. The value of f = 0.3 and t = 0.005 were chosen for both pairs.

Table 5.4: DS_b parameter experimentation for displacement maps from pair I and pair II.

Distance threshold (t)	Time taken for simulation (S)	RMSE (m)	
		Pair I	Pair II
0.05	5867	0.01264	0.01402
0.03	26211	0.00835	0.01027
0.01	53859	0.00485	0.00761
0.005	67156	0.00454	0.00745
Scan Fraction of TI (f)	Time taken for simulation (S)	RMSE (m)	
		Pair I	Pair II
0.2	6208	0.01270	0.01406
0.3	6317	0.01264	0.01402
0.4	6825	0.01264	0.01402
0.5	8202	0.01264	0.01402
0.6	8379	0.01264	0.01402
Number of nodes (n)	Time taken for simulation (S)	RMSE (m)	
		Pair I	Pair II
5	450	0.01297	0.01304
10	1237	0.01255	0.01268
15	1877	0.01244	0.01292
20	3257	0.01272	0.01329

Table 5.5 summarizes the best parameters obtained from experimentation for the DS_u and DS_b simulations. The combination of the best parameters found by experimentation was used for final 10 unconditional simulations. The DS method is not a deterministic approach so 10 stochastic realizations were generated, which means for each gapped pixel 10 possible displacement values were simulated. The mean of the 10 simulated values were taken as final result and used for validation and filling up the missing displacement values inferred from pair I and pair II. The accuracy assessment results of DS_u and DS_b gap filling for both pairs are in section 5.4.3.

Table 5.5: The best parameters used for reconstruction of the displacement maps shown in Figure 5.3. The result after reconstruction is shown in Figure 5.12 and Figure 5.13 for pair I and pair II respectively.

Displacement Map	Number of nodes (n)	Scan Fraction (f)	Distance threshold (t)	Number of realizations	Time taken for 10 simulations (Hrs)	
					Univariate	Bivariate
Pair I	15	0.3	0.005	10	56	97 (Both pairs together)
Pair II	10	0.3	0.005	10	43	

5.4.3. Quantitative measures of error

The predicted values were compared with the original values at the 12 shifted polygons scattered in different locations for validation of OK and DS methods. The RMSE of the three cases for both pairs are given in Table 5.6. The lower value of the RMSE is the better. The RMSE of both DS cases are much smaller than that of OK. The RMSE of both DS cases are over 50% lower than OK. Between DS_u and DS_b, the RMSE of DS_u is lower, with slight improvement.

Table 5.6: Validation results—RMSE of OK prediction, DS_u and DS_b cases.

	RMSE		
	OK Prediction	DS Univariate	DS Bivariate
Pair I	0.00651	0.00213	0.00316
Pair II	0.00495	0.00164	0.00241

In the scatterplots for pair I and pair II presented in Figure 5.7 and Figure 5.8 respectively, the measured values were plotted against the reference values. It can be seen that all points fall in and around the reference line (shown in red) of slope 1 and intercept 0. Few points with higher displacement values spread away from the reference line. The scatter of OK is greater than that of both DS_u and DS_b. Between DS_u and DS_b, the scatter of DS_u is slightly narrower. Hence, DS_u case showed the narrowest scatter.

The histogram of residuals for pair I and pair II are presented in Figure 5.7 and Figure 5.8 respectively. The residuals were calculated by subtracting the reference values from the measured values. All histograms clearly show steeper and symmetrical distribution—with the two DS cases appearing narrower and more normally distributed. For all three cases, most of errors are concentrated in and around 0 and are mostly unbiased. For OK, the (95%) most of the errors in the displacement values are within the range of [-0.015 m, +0.015 m], while the corresponding range for DS_u and DS_b is [-0.005 m, +0.005 m], with DS_u having the steepest distribution than OK prediction and DS_b simulation.

From quantitative perspective, both DS cases demonstrated better prediction compared to OK. Among the two DS cases, DS_u simulation showed slight improvement in reconstruction accuracy compared to DS_b simulations for both pairs.

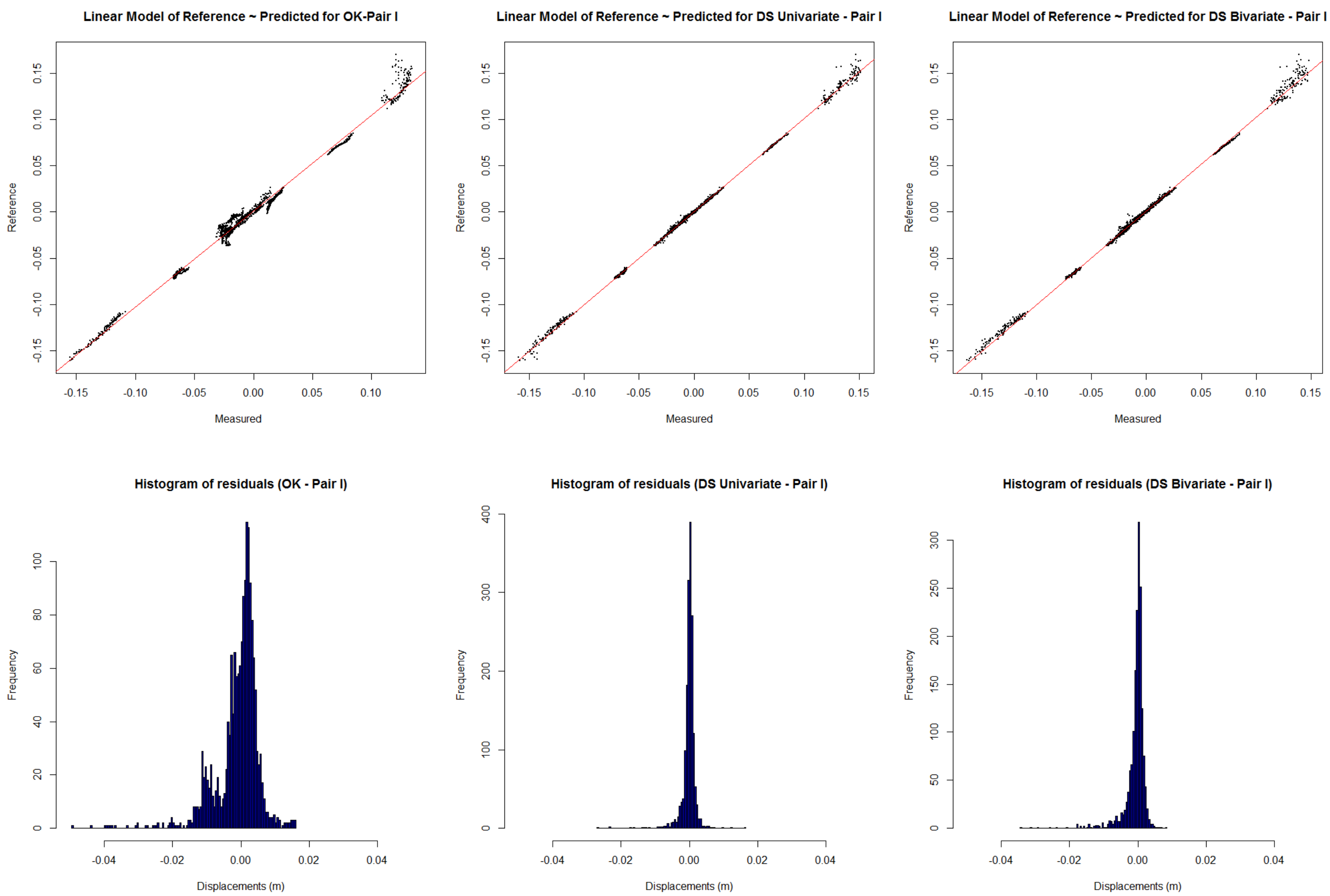

Figure 5.7: Scatterplots (top) of reference versus measured displacement values with fitted reference line in red and histograms of residuals (bottom) of all three cases (from left to right)—OK, DS_u and DS_b—for displacements from pair I.

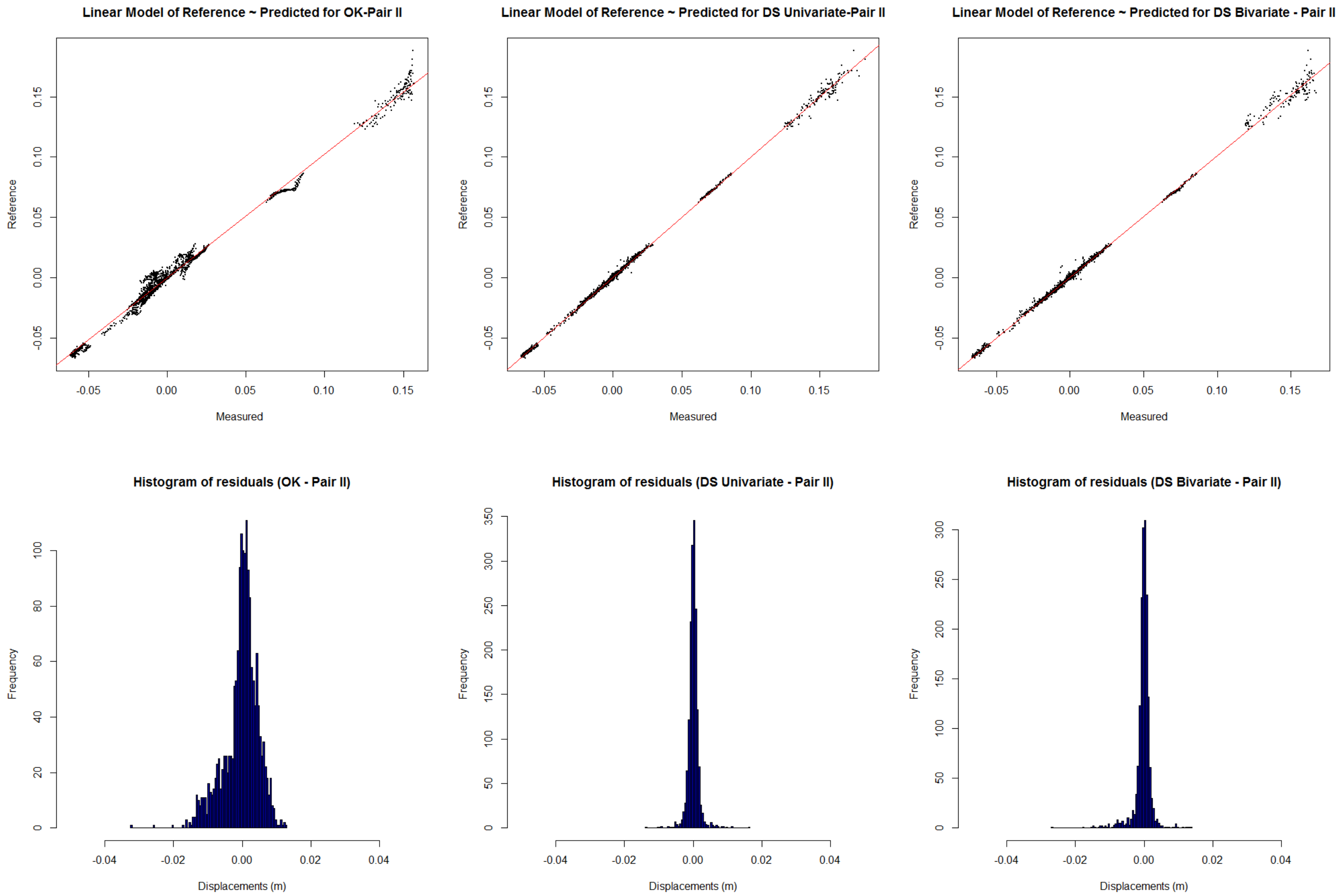

Figure 5.8: Scatterplots (top) of reference versus measured displacement values with fitted reference line in red and histograms of residuals (bottom) of all three cases (from left to right)—OK, DS_u and DS_b—for displacements from pair II.

5.5. THREE SHIFTED POLYGONS

5.5.1. Ordinary Kriging

The adopted sampling strategy to calibrate the variogram model was same as of 12 shifted polygons (see sub-section 5.4.1). The variograms for displacement variables for three shifted polygons from pair II are given in Table 5.7. The Exponential variogram, presented graphically in Figure 5.9, is the best fitted authorized model for three shifted polygons with least SSE. For all three shifted polygons, the structure of the spatial dependency of the displacements was modelled by Exponential variogram. The fitted variograms had very small nugget value (close to 0) meaning that the spatial variability is strongly correlated in space legitimizing the use of OK prediction.

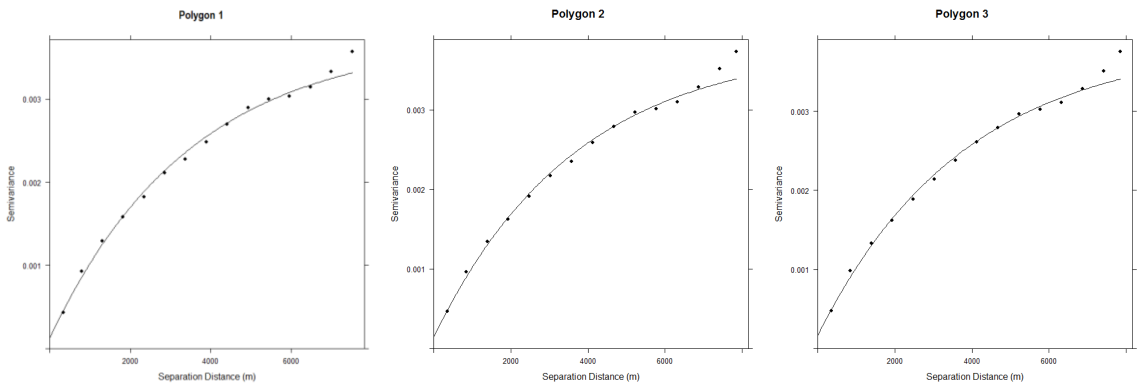

Figure 5.9: Fitted variogram (OK) for three shifted polygons. Variogram names and their parameters are shown in Table 5.7.

Missing displacement values of the three shifted polygons were interpolated using the modelled variogram. The validation results—RMSE of the interpolated displacement values are shown in Table 5.8. Further accuracy assessment indicators, histograms of residuals and scatterplots of reference versus measured values are shown in Figure 5.10.

Table 5.7: Variograms for OK of displacements from image pair II for three shifted polygons. The fitted variograms are shown graphically is Figure 5.9.

	Fitted Variogram				
	Model	Range	Sill	Nugget	SSE
Polygon 1	Exponential	3567.60	3.78×10^{-3}	1.28×10^{-4}	5.14×10^{-9}
Polygon 2	Exponential	3745.42	3.56×10^{-3}	1.58×10^{-4}	7.33×10^{-9}
Polygon 3	Exponential	3798.86	3.71×10^{-3}	1.64×10^{-4}	4.93×10^{-9}

5.5.2. Direct Sampling

The fine-tuned parameters for displacement values from pair II given in Table 5.5 were used to generate 10 stochastic realizations of the displacement values in the three shifted polygons. The average of the 10 simulated values corresponding to each missing pixel was taken as final result, and was used for validation and filling up the corresponding missing value. The accuracy assessment results of DS_u gap filling of displacement values from pair II in three shifted polygons are presented in section 5.5.3.

5.5.3. Quantitative measures of error

Accuracy assessment in terms of RMSE for OK and DS_u for the three shifted polygons in a key location (see Figure 5.4) is given in Table 5.8. The RMSE of DS_u is significantly smaller than that of OK for all three shifted polygon. With the increase in the gap size the accuracy degrades for both OK and DS_u. Yet,

DS_u results are still more accurate than OK. With growing gap sizes, the drop in RMSE for OK is sudden; while for DS_u is small and gradual. The difference in RMSE (OK minus DS_u) increases with increasing gap size. This suggests OK performance for small gaps are satisfactory but with increasing gap size OK is unable to perform accurate prediction. On the contrary, DS_u performs accurate prediction even with increasing gap sizes.

Table 5.8: Validation results – RMSE of OK prediction and DS_u cases.

	RMSE		RMSE difference
	OK Prediction	DS Univariate	(OK – DS_u)
Polygon 1	0.00369	0.00063	0.00306
Polygon 2	0.00845	0.00141	0.00704
Polygon 3	0.00834	0.00221	0.00613

The scatterplots of OK and DS_u for all three shifted polygons presented in Figure 5.10 shows that all points lie in and around the reference line (shown in red) of slope 1 and intercept 0 for DS_u whereas the point spread further away from the reference line and the reference line deviation from slope 1 and intercept 0 for OK. The scatter from polygon 1 to polygon 3 increased significantly for OK. Even though the scatter from polygon 1 to polygon 3 increased for DS_u, it is very slight relative to OK.

The histogram of residuals of OK and DS_u for all three shifted polygons shown in Figure 5.10 clearly shows steeper, symmetrical and narrower distribution for DS_u than OK. In case of OK, the range of the errors in the displacement values from polygon 1 to polygon 3 increased notably. In contrast, most of the errors in the displacement values are within range of [-0.005, +0.005] for DS_u.

All the accuracy assessment indicators suggested that the performance of DS_u is superior to OK with growing gap sizes.

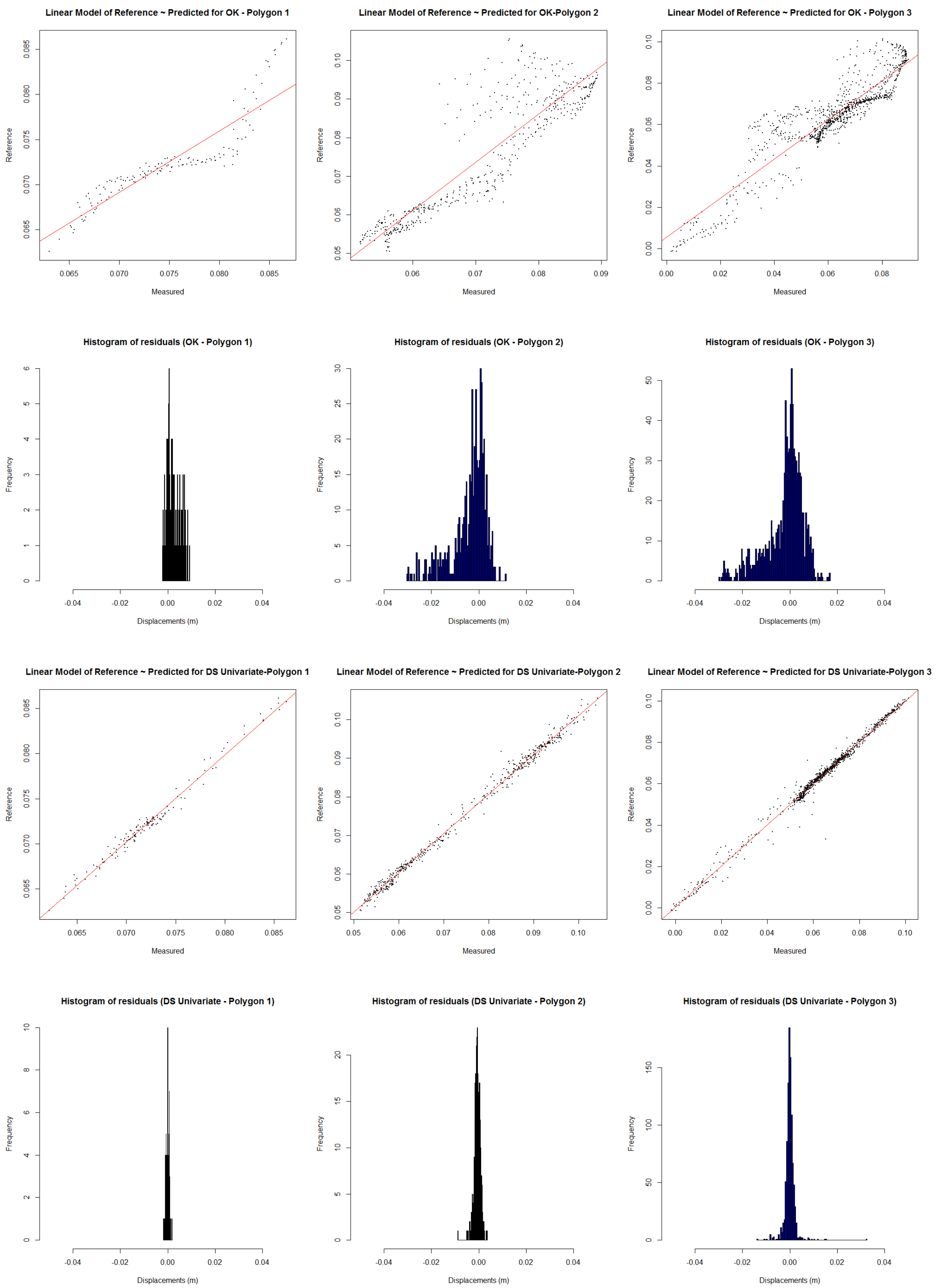

Figure 5.10: Scatterplots (top) of reference versus measured displacement values with fitted reference line in red and histograms of residuals (bottom) of OK and DS_u for displacements from pair II. The three columns represent graphs for polygon 1 to polygon 3 (from left to right).

5.5.4. Qualitative assessment

The spatial distribution of residuals for three shifted polygons can be clearly seen in Figure 5.11, which displays the residuals of OK and DS_u, and the difference in residual magnitudes of OK and DS_u. In the residual maps of OK, some area in all three polygons have zero residuals (green) with increasing positive residuals (yellow to red) and negative residuals (cyan to blue) from polygon 1 to polygon 3. The negative residuals indicate underestimation of displacements whereas positive residuals imply overestimation. The occurrences of negative residuals are higher meaning areas of underestimation are high. On the contrary, in the residual maps of DS_u, most of the areas in all three polygons have zero residuals with few positive and negative residuals, especially in polygon 3.

With increasing gap size from polygon 1 to polygon 3, the residuals of OK and DS_u increased, with OK showing significant rise in residual values. For all three shifted polygons, the residuals of OK are greater than that of DS_u.

The maps showing the difference in residual magnitudes of OK and DS_u mostly reveals neutral (green) and positive areas (yellow to red)—where DS_u outperforms OK.

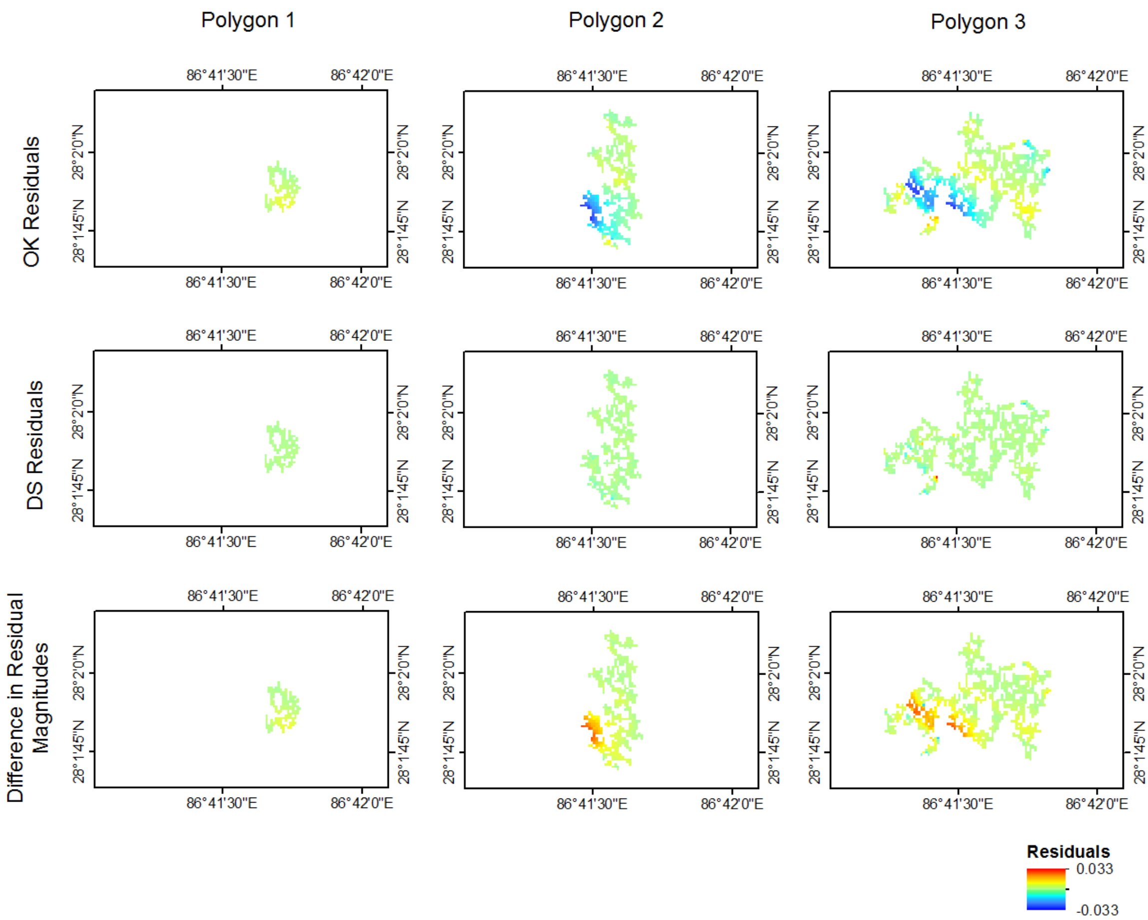

Figure 5.11: Residual distribution maps of the reconstructions in three shifted polygons. The three columns represent three shifted polygons (from left to right)—polygon 1, polygon 2 and polygon 3. The first two rows describe the residuals of OK (the predicted minus the actual displacements) and the residuals of DS (the mean of the reconstructed minus the actual displacements). The last row shows the difference in residual magnitude (absolute value of the residuals of OK minus the absolute value of the residuals DS).

5.6. DISPLACEMENT MAPS

By combining the predicted results of the missing displacement values with the known values of the glacial displacement map for all three cases—OK, DS_u and DS_b—complete glacial displacement maps were produced. The prepared displacement maps from pair I and pair II are shown in Figure 5.12 and Figure 5.13 respectively.

To better compare the quality of gap filling of all three cases, a small portion of the filled displacement map from pair I and pair II was enlarged and presented at the bottom of Figure 5.12 and Figure 5.13 respectively. Some noises were seen in the OK interpolated displacement map whereas the results from DS were relatively smooth. DS maps showed better preservation of the glacier displacement patterns than OK. DS_u and DS_b filled displacement maps are both similar, with some subtle differences. This visual qualitative assessment concurs with the error statistics, with DS providing better gap filling results.

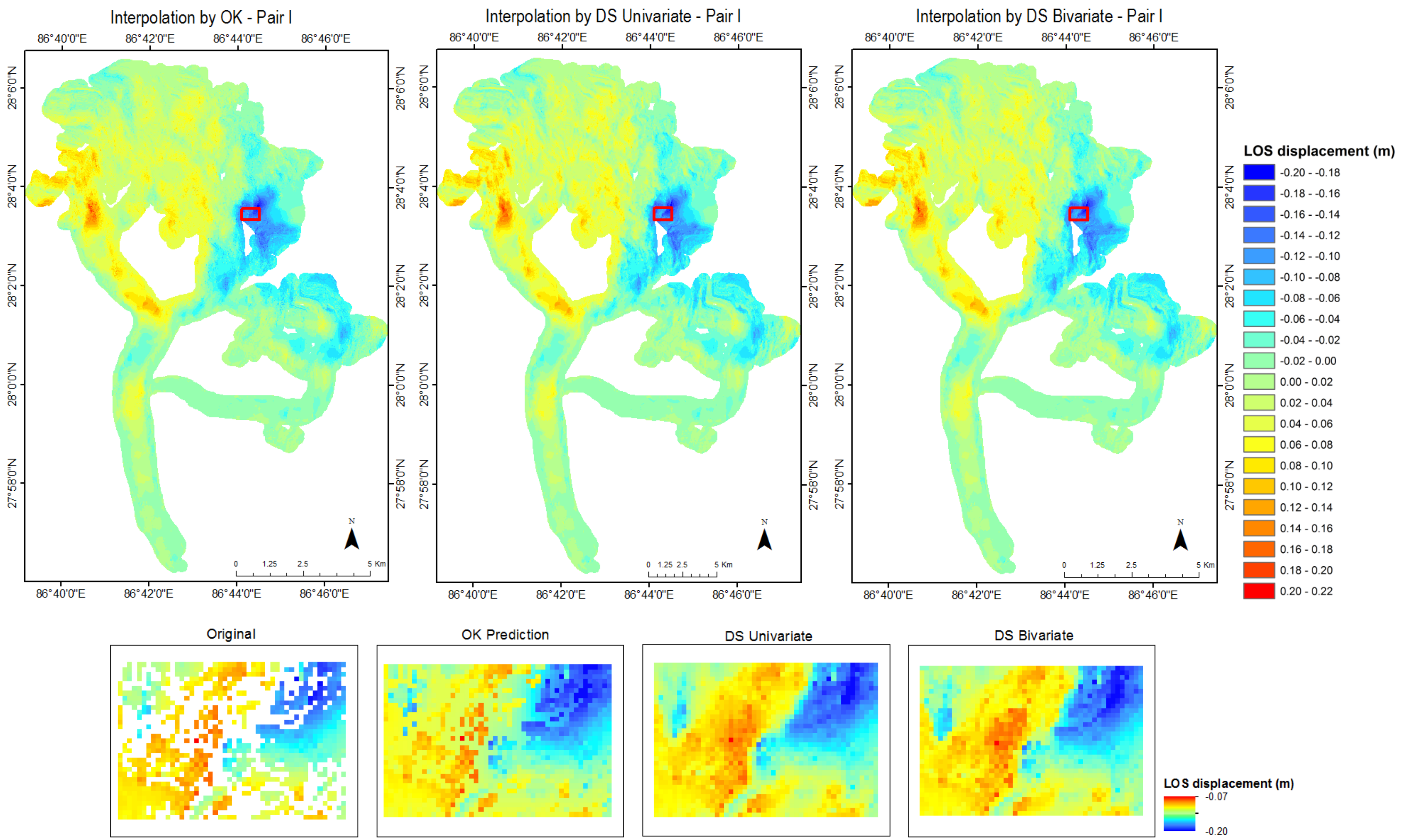

Figure 5.12: The reconstructed displacement map (pair I) of Figure 5.3(a) using the parameters shown in Table 5.2 for OK prediction and Table 5.5 for both DS_u and DS_b simulation (top). The red box (top) defines the bounds of a zoomed subset (bottom) of the original gapped displacement map and filled displacement maps for OK, DS_u and DS_b (from left to right).

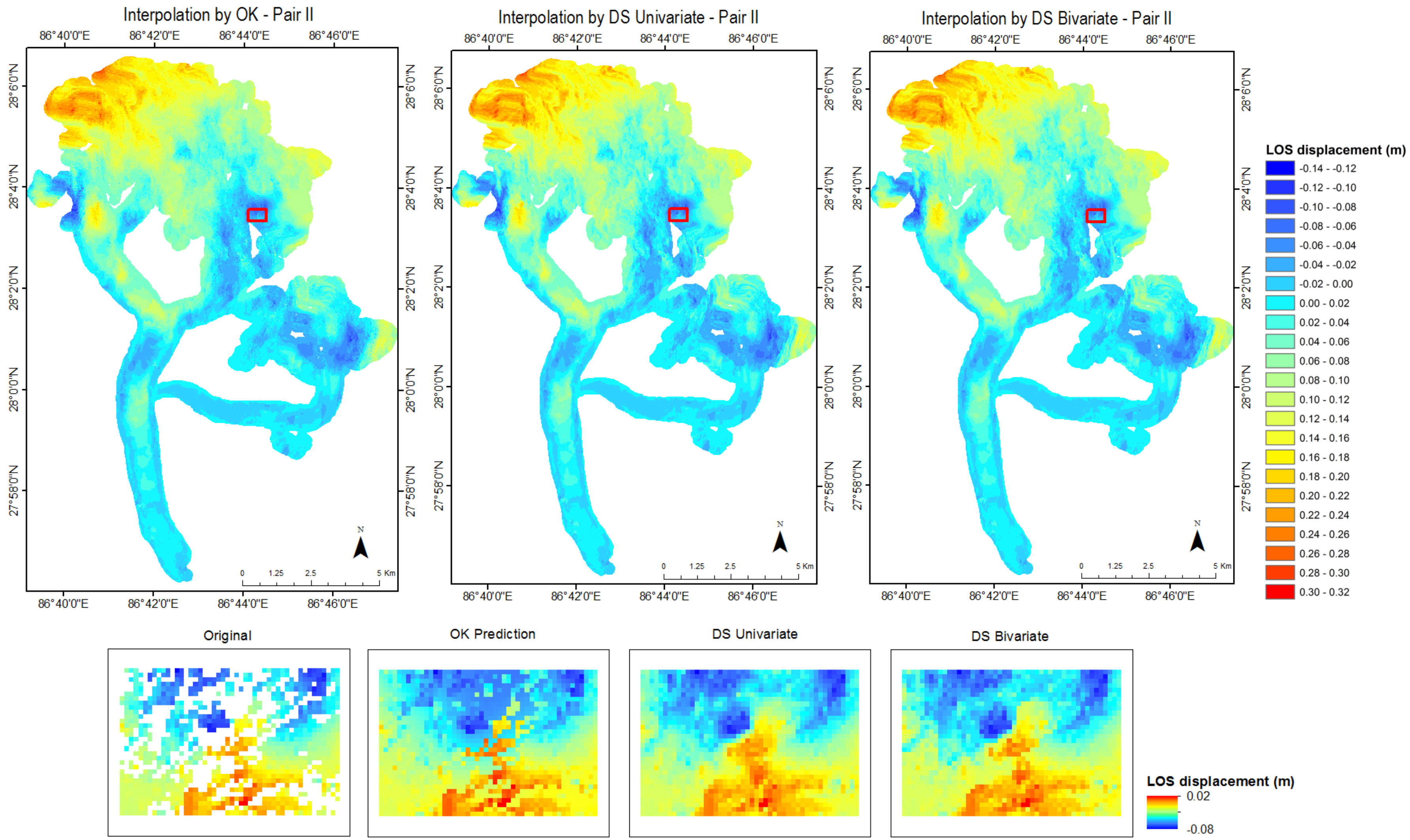

Figure 5.13: The reconstructed displacement map (pair II) of Figure 5.3(a) using the parameters shown in Table 5.2 for OK prediction and Table 5.5 for both DS_u and DS_b simulation (top). The red box (top) defines the bounds of a zoomed subset (bottom) of the original gapped displacement map and filled displacement maps for OK, DS_u and DS_b (from left to right).

6. DISCUSSION

In the first section of this chapter, the results of the DInSAR inferred glacier displacement maps are discussed. In the succeeding section, the analysis carried out for the performance evaluation of the gap filling of OK and DS are presented.

6.1. DINSAR

This study demonstrated the use of novel S1 SAR data for deriving the glacier displacement map using DInSAR.

Changes in the glacier surface are less intense during the winter period of the year which is why most of the successfully analysed interferograms are presenting data on period of lower glacial displacement than during the summer season (Perski et al., 2004). The same case occurred in this research. Interferograms were constructed from S1 SAR image pairs throughout the year of 2015 and 2016. The temporal separation of the image pairs were 6-days, 12-days, 24-days and 36-days. All interferograms were analysed but none of them with time interval of 12-days and above were coherent. Thus, they were excluded from the study. The coherent image pairs were found in the months of November and December 2016, when the temperature and sun-illumination are low and the displacement gradient is minimal. These were also the first S1 image pairs of the study area with 6-day repeat orbits found in ESA's archive.

The displacement pattern over whole Ngozumpa glacier was calculated and assessed. In previous work by Quincey et al. (2009), no flow is recorded in the lowermost 6.5 km of the tongue of Ngozumpa Glacier. This report fits with the findings of this study. In the terminus, the glacier displacement close to zero was found and the active part of the glacier is several kilometres from the terminus (see Figures 5.2(a) and 5.2(b)).

The western tributary is very active with rapidly increasing displacement than the eastern tributary. The other major tributary feeding from the east, Garuna (see Figure 3.1) is no longer dynamically connected to Ngozumpa glacier. These observations matched with the study carried out by Benn et al. (2000). The observed spatial variation and pattern of interferometry derived LOS displacement agrees with the previously carried out studies using ERS Tandem images by Quincey et al. (2009). No direct field based validation was performed. However, comparative validation with the previous studies of the Ngozumpa glacier shows that the DInSAR results are realistic. The DInSAR technique is highly accurate and can be applied to retrieve displacement field of mountain glacier, despite the difficulties of rugged topography.

6.2. OK AND DS GAP FILLING

Geostatistical methods—especially OK—have been proposed to fill the missing displacement values inferred from DInSAR. In this study, the newly developed geostatistical DS method has been implemented to fill the missing values in DInSAR derived displacement maps.

For OK, experimental variograms were approximated using best fitting theoretical models. The interpolation results from variograms with small nugget are more accurate than those with larger nugget (Karl, 2010). The variogram models used for interpolating missing values in displacement maps form pair I and pair II, had small nugget values. This indicates that the data are highly correlated in space and semivariance is more useful for predicting missing values.

The three user defined parameters t, n and f were fine-tuned for each DS case individually. Setting t=1, DS samples the TI unconditionally without any spatial dependence constraints, and therefore only the marginal distribution of Z is reproduced. Conversely, setting t=0, an exact match between the data event in the SG and the one of the TI is sought. This would mean that the spatial pattern in the TI is reproduced with the highest possible accuracy. As displacement data is a continuous variable, an exact match is nearly impossible to find. For this reason, an acceptable threshold t close but not equal to 0 needs to be defined. Also, to avoid a verbatim copy of the TI, t should not be 0. Further, CPU time increases with decreasing values of t. The maximum number of nodes n controls the size of the data event. Large values of n expand the size of data events resulting in small search windows. Therefore, only the statistical properties of a small central portion of the TI are reproduced resulting in unimproved simulation quality. Finally, for the maximum scan fraction *f*, it is observed that for $f \leq 0.2$, the simulation quality degraded because the probability of finding matching TI pattern is lower. Even with the increase of *f* from 0.3 to 1.0, the RMSE value remained the same, meaning that DS is able to find a matching pattern by scanning less or equals to 0.3 of the TI but the computational cost increases. Hence, variations in *f* have little effect on the simulation quality. These observations fit with those of Meerschman et al. (2013) that for the continuous cases f has little influence on the simulation quality, and decreasing t results in a substantial decrease in CPU time without a large decrease in simulation quality. The use of one-third scan fraction further insures that different parts of the TI are scanned during simulation of different nodes, which avoids verbatim copy. Additionally, the conditioning data helped in avoiding the verbatim copy (Meerschman et al., 2013). In summary, the selection of the optimal parameters for DS simulations depends upon the trade-off between the CPU time and simulation quality.

The quality of OK, and of DS_u and DS_b reconstructions were assessed by validating against reference values for 12 shifted artificial polygons enforced at different locations. The two DS cases gave better results than OK for displacements from both image pairs. This can be attributed to the ability of DS to capture internal heterogeneity and multiple point dependencies of the glacier displacement field.

Applying multivariate multiple-point relationships, gaps in multiple variables can be reconstructed accurately using multiple incomplete covariates, provided that the additional information added by the auxiliary variables are complementary (Mariethoz et al., 2012). Bivariate simulation offers improved prediction when compared with univariate simulation if information provided by the co-variate is complementary (Yin et al., 2015). The results of DS_u and DS_b were similar, with DS_u providing slight improvements against DS_b. This may be attributed to the insufficient complementarity of the displacement characteristics of two maps (high temporal variability). Therefore, the additional data provided were not informative enough to outperform DS_u. Still, DS_b is advantageous as multiple displacement maps can be filled jointly preserving the linear and non-linear relationship between them.

DS is known for its ability to reconstruct larger gaps. Three selected polygons of increasing size were shifted to a key location to assess the performance of DS with the increase of the spatial extent of the gaps. The reconstruction results of the three shifted polygons of increasing size shows that the accuracy degrades for both DS and OK if gap size grows. The entire spatial structure may be missing in large gaps causing the reconstruction to be less accurate. Nevertheless, DS performed better than OK for large gaps, with only a slight drop in performance. The abrupt decrease in the performance of the OK is due to the increase in the degree of spatial heterogeneity in large gap sizes. Some structures present on either side of the small gap facilitate gap filling with realistic values (Mariethoz et al., 2012). Thus, OK gave good results for small gaps, whereas it cannot reproduce complex spatial patterns of large gaps (Journel & Zhang, 2007; Olea & Pawlowsky, 1996). In contrast MPS is able to resolve complex spatial patterns even in large gap sizes where OK fails. Thus, DS results are superior to OK with growing gap sizes.

RMSE values showed that the accuracy of gap filling of DS were at the mm scale, whereas precision of DInSAR is at the cm scale. Thus, the obtained accuracy of gap filling by DS is acceptable and below the detection limit of DInSAR technique.

A prominent advantage of an MPS technique like DS as compared with conventional geostatistical methods like Kriging is that it is straightforward to implement. In this study, OK was performed for the entire displacement map at once, whereas OK performs better locally. For local interpolation, the displacement map should be divided into patches. Some research divides a study area manually into contiguous patches with sufficient sample points (Yaseen et al., 2013). For each patch, an independent variogram analysis is performed during which an experimental variogram is calculated and best fitting theoretical model is selected. With numerous patches formed, this process is theoretically as well as computationally challenging. In contrast, MPS is simpler with its key concept of sampling spatial patterns from within TIs for predicting unknown values.

For DS, the mean of 10 realizations of reconstruction results was presented. Since all reconstructed values are equally probable, the multiple realizations can estimate the uncertainty associated with the reconstructions which are not provided by other deterministic reconstruction methods. A Monte Carlo framework can be implemented to estimate the uncertainty relate to multiple reconstructions (Jha et al., 2013; Mariethoz et al., 2012).

Another advantage of the DS over OK is the reduced computational burden. If the number of sample points and the number of weighting coefficients become very large in OK, the covariance matrix grows as well, resulting in a computationally expensive matrix inversion. Taking 5100 samples for calibration, OK prediction took almost 44.5 hours using on a windows computer with an Intel Core 2.50 i7 GHz processor and 8 GB of RAM to reconstruct the gaps in the displacement map from pair II. Using the same computer, DS_u took 43 hours to fill gaps in the same displacement map. If all known displacement values were taken to calibrate with OK, inversion of the resulting large covariance matrix would require a computational cost several times greater than that of DS simulations.

Most of the proposed gap filling methods are limited to only one unknown variable to be reconstructed (Mariethoz et al., 2012). DS demonstrated the potential of bivariate simulation. The conditioning data for both variables (here displacement values from pair I and II) were honoured. Only DS has the capability to perform bivariate and multivariate simulations among the MPS methods till date. Further, conventional geostatistical methods are not capable to perform gap filling in a bivariate and multivariate environment.

7. CONCLUSION AND RECCOMENDATION

7.1. CONCLUSION

This study concludes that a novel S1 SAR dataset can be successfully used to retrieve the surface displacements of a mountain glacier employing a well-established DInSAR technique. Despite the rugged terrain and inaccessibility, due to free availability of high quality SRTM DEM and precise orbital data from POD services, DInSAR yielded valuable surface displacement information with comparatively little other external input. Since S1 datasets have a worldwide coverage, glacier monitoring can be carried out at regional and global scales at medium resolution. The 6 day repeat pass S1 dataset is a valuable resource for seasonal variability studies of glacier displacement fields.

Missing values in glacier displacement map inferred from DInSAR, mainly due to decorrelation of SAR images have to be reconstructed. This research demonstrated the implementation of DS univariate and bivariate techniques, a newly developed MPS. The parameters were fine tuned for univariate and bivariate cases, and their effects on the performance were analysed. Performance of DS was evaluated against OK—a conventional geostatistical method. In both qualitative and quantitative assessment, DS performed better than OK. A requirement for using MPS is selection of a suitable TI. Even when using the information contained within the non-gapped area of the displacement map to be reconstructed, DS provided acceptable results, well below the detection limit of DInSAR technique. This study concludes that DS can be successfully used for deriving missing displacement values in a glacier.

The answers to the research questions posed in the first chapter are provided below:

1. *Which MPS method is most suitable to reconstruct the missing surface displacement values inferred from DInSAR?*

   From comparative analysis of the state-of-art MPS methods and related works concisely reviewed in Chapter 2, DS was chosen for the reconstruction of gaps in the displacements derived from DInSAR.

   The surface displacement values inferred from DInSAR are continuous. DS is a pixel-based MPS method that can simulate continuous variable employing training images (TIs) that can be fully or partially informed. DS applies a distance threshold (t) for pattern matching. The simplicity of the distance concept of DS effectively avoids the use of multi grid to capture spatial structures of all sizes, avoids the need to construct pattern database prior to simulation, allows an easy data conditioning, performs multivariate simulation, and a joint simulation of multiple categorical and continuous variables. Since DS has no need to catalogue patterns found in TIs, the memory requirement and CPU time are reduced largely. For these reasons, DS is better than other MPS methods for this study.

2. *What are the optimal parameter settings for implemented MPS method to obtain the best pattern reproduction?*

   The simulation quality of DS highly depends upon the three main user defined parameters—the distance threshold (t), the maximum scan fraction of TI (f) and the maximum number of nodes in the neighbourhood (n). For every particular case, the optimal values of these three parameters need to be fine-tuned. In general, decreasing t and increasing n and f result in improved simulation quality. However, due to these settings first, the CPU time grows and second, verbatim copies of part of TI may occur in simulation results. By choosing $f < 1$ and a slight relaxation of t and n values, verbatim copies can be avoided and computational cost can be reduced significantly. Thus, the choices should balance between available CPU time and simulation quality. The choices made regarding the fixed parameters and the reasons for their selection have been discussed in detail in sub-section 4.3.

3. *How can fully informative training images (TIs) be made for reconstruction of pattern and spatial structure in the gaps?*

As long as TIs capture the spatial variability both at coarse and fine-scale of the missing areas, the size of TIs is not of concern. TIs can be smaller or bigger or same size as the target image to be filled. The choice of fully informative TIs is not straightforward. TIs can be taken from a TI database built for gaps in glacier displacement maps. TIs can come from another glacier area with a spatial structure and pattern resembling the study area. Hand drawn TIs or synthetic TIs guided by expert knowledge can also be built. For our study, these options are not available and therefore custom made TIs suiting the application were constructed.

The partially gapped displacement map generated from the DInSAR itself can serve as TI. This is only possible due to capability of DS to simulate with an incomplete TI. The information from the non-gapped area of the displacement map comprises of the spatial variability and structure of the glacier displacement phenomenon. Thus, the use of non-gapped area of the displacement map itself as TI is informative enough for gap filling. Even if a valid TI is employed, the results will not be accurate without conditioning data. They work as a control to constrain the simulation and to guide the pattern replication. Thus, the use of known portion of the displacement map as conditioning data further improved the reconstruction of pattern and spatial structure in the gaps. Other potential TIs are the displacement maps generated on the same season from other SAR image pairs.

4. *What are the effective methods for assessment of the reconstructed results in the missing area?*

The reconstructed results of the missing values were evaluated using several performance measures: RMSE, histogram of residuals, scatterplot of the reference versus interpolated displacement values and residuals maps. Even though RMSE is a frequently reported accuracy assessment measure, it is sensitive to occasional large errors. Ranking performance solely on the RMSE might not suffice. Thus, histogram of residuals and scatterplots of reference versus simulated values were also employed. The first three measures were used for quantitative assessment while the visual inspection of the distribution of the residuals in residuals map provided qualitative assessment of the reconstruction results of both OK and DS.

5. *Which conventional geostatistical method is appropriate for benchmarking the MPS results?*

Out of numerous conventional geostatistical methods, OK is the most established method in literature. It performs superior interpolation compared to deterministic methods like IDW and spline. OK uses the variogram to model the spatial dependencies. There are other kriging methods like Universal Kriging (UK), Indicator Kriging (IK) and Co-kriging (CK). OK, however, is widely used and utilizes the simplest model to capture spatial dependencies by assuming constant unknown mean. This is a valid assumption unless trend occurs in the data. Literature showed that OK has been successfully used for deriving missing values in LOS displacement map inferred from DInSAR (see Chapter 2). Thus, OK is the appropriate geostatistical method for benchmarking MPS results.

6. *Does MPS perform better gap filling compared to the conventional geostatistical method? If yes, in which aspect of performance measures is MPS superior to conventional geostatistical method?*

   The comparative performance analysis of DS with OK clearly showed that MPS results in more accurate gap filling. In all employed quantitative measures of performance DS performed better than OK, with improvement of more than 50 %. Also, the visual inspection of the reconstructed displacement maps and distribution of residuals concur with the quantitative assessment. Further superiority of MPS is its reduced computational cost and straightforward implementation as compared to conventional geostatistical methods. Even non-expert users can easily understand and use MPS because it does not require complex theoretical background and assumptions such as positive definite covariance matrices and variography needed for conventional geostatistical methods. Another outstanding feature of DS is its provision of multivariate gap reconstruction which none of the conventional geostatistical method provide.

7.2. RECOMMENDATION

At last, few recommendations for the future research are provided:

- One limitation faced during this research is the availability of few coherent S1 SAR image pairs from which DInSAR based displacement maps could be generated. Two coherent image pairs were available till the commencement of this research, so the TIs were limited to only two displacement maps. Since then, S1 database has grown so has the prospect of number of coherent image pairs for glacier displacement analysis. With the increasing availability of S1 SAR data of a 6 day temporal baseline, maintaining coherence between the image acquisitions is not difficult as before. In future work, large number of displacement maps can be supplied as TIs. Use of large training set (multiple TIs) can offer better reconstruction results given the rich supply of spatial patterns.
- Even though this study was limited to bivariate simulation, DS can easily be extended to multivariate simulations. Missing values in multiple DInSAR derived glacier displacement maps can be filled together preserving even non-linear dependencies between the variables considered. Seasonal variability is observed in glacier displacement phenomenon. Provided the displacement images of same season, the temporal variability is very small and therefore the data are complementary. So, multivariate simulation might have better performance than the univariate simulation. The spatio-temporal gap reconstruction in seasonal basis might provide promising results.
- The LOS displacements with spatial discontinuities removed using DS can be converted into the glacier surface 3D velocity field. However, due to time constraints, it was not possible in this research. Another possible direction for future research, both the ascending and descending mode DInSAR results can be combined to obtain 3-dimentional velocity field. Assuming surface parallel flow, the LOS displacements can further be converted to the horizontal velocity.

LIST OF REFERENCES

Addink, E. A. (1999). A comparison of conventional and geostatistical methods to replace clouded pixels in NOAA-AVHRR images. *International Journal of Remote Sensing*, *20*(5), 961–977. http://doi.org/10.1080/014311699213028

Alsdorf, D., Birkett, C., Dunne, T., Melack, J., & Hess, L. (2001). Water level changes in a large Amazon lake measured with spaceborne radar interferometry and altimetry. *Geophysical Research Letters*, *28*(14), 2671–2674. http://doi.org/10.1029/2001GL012962

Amelung, F., Jonsson, S., Zebker, H., & Segall, P. (2000). Widespread uplift and "trapdoor" faulting on Galapagos volcanoes observed with radar interferometry. *Nature*, *407*, 993–996. http://doi.org/10.1038/nature01526.1.

Arpat, G. B., & Caers, J. (2007). Conditional Simulation with Patterns. *Mathematical Geology*, *39*(2), 177–203. http://doi.org/10.1007/s11004-006-9075-3

Askne, J. I. H., Dammert, P. B. G., Ulander, L. M. H., & Smith, G. (1999). C-band repeat-pass interferometric SAR observations of the forest. *Doktorsavhandlingar Vid Chalmers Tekniska Hogskola*, *35*(1547), 25–35. http://doi.org/10.1109/36.551931

Baldi, A. (2003). Phase unwrapping by region growing. *Applied Optics*, *42*(14), 2498. http://doi.org/10.1364/AO.42.002498

Balzter, H., Rowland, C. S., & Saich, P. (2007). Forest canopy height and carbon estimation at Monks Wood National Nature Reserve, UK, using dual-wavelength SAR interferometry. *Remote Sensing of Environment*, *108*(3), 224–239. http://doi.org/10.1016/j.rse.2006.11.014

Benn, D. I., Wiseman, S., & Warren, C. R. (2000). Rapid growth of a supraglacial lake, Ngozumpa Glacier, Khumbu Himal, Nepal. In M. Nakawa, C. F. Raumond, & A. Fountain (Eds.), *Debris-covered Glaciers* (pp. 177–186). Seattle, Washington, USA: International Society of Hydrological Sciences.

Berardino, P., Fornaro, G., Lanari, R., & Sansosti, E. (2002). A new algorithm for monitoring localized deformation phenomena based on small baseline differential SAR interferograms. In *IEEE International Geoscience and Remote Sensing Symposium* (Vol. 2, pp. 1237–1239). IEEE. http://doi.org/10.1109/IGARSS.2002.1025900

Berthier, E., Vadon, H., Baratoux, D., Arnaud, Y., Vincent, C., Feigl, K. L., … Legrésy, B. (2005). Surface motion of mountain glaciers derived from satellite optical imagery. *Remote Sensing of Environment*, *95*(1), 14–28. http://doi.org/10.1016/j.rse.2004.11.005

Bhattacharya, A., Arora, M. K., & Sharma, M. L. (2012). Usefulness of synthetic aperture radar (SAR) interferometry for digital elevation model (DEM) generation and estimation of land surface displacement in Jharia coal field area. *Geocarto International*, *27*(1), 57–77. http://doi.org/10.1080/10106049.2011.614358

Bivand, R., Keitt, T., & Rowlingson, B. (2016). rgdal: Bindings for the Geospatial Data Abstraction Library. R package version 1.2-4. Retrieved from https://cran.r-project.org/package=rgdal

Björnsson, H., Rott, H., Gudmundsson, S., Fischer, A., Siegel, A., & Gudmundsson, M. T. (2001). Glacier–volcano interactions deduced by SAR interferometry. *Journal of Glaciology*, *47*(156), 58–70. http://doi.org/10.3189/172756501781832520

Boisvert, J. B., Pyrcz, M. J., & Deutsch, C. V. (2007). Multiple-Point Statistics for Training Image Selection. *Natural Resources Research*, *16*(4), 313–321. http://doi.org/10.1007/s11053-008-9058-9

Caers, J., & Journel, A. G. (1998). Stochastic Reservoir Simulation Using Neural Networks Trained on Outcrop Data. In *SPE Annual Technical Conference and Exhibition* (p. 16). New Orleans: SPE 49026:Society of Petroleum Engineers. http://doi.org/10.2118/49026-MS

Chen, C. W., & Zebker, H. A. (2002). Phase unwrapping for large SAR interferograms: statistical segmentation and generalized network models. *IEEE Transactions on Geoscience and Remote Sensing*, *40*(8), 1709–1719. http://doi.org/10.1109/TGRS.2002.802453

Colesanti, C., & Wasowski, J. (2006). Investigating landslides with space-borne Synthetic Aperture Radar (SAR) interferometry. *Engineering Geology*, *88*(3–4), 173–199. http://doi.org/10.1016/j.enggeo.2006.09.013

Costantini, M. (1998). A novel phase unwrapping method based on network programming. *IEEE Transactions on Geoscience and Remote Sensing*, *36*(3), 813–821. http://doi.org/10.1109/36.673674

Cressie, N. A. C. (1993). *Statistics for Spatial Data*. Hoboken, NJ, USA: John Wiley & Sons, Inc. http://doi.org/10.1002/9781119115151

Curran, P. J., & Atkinson, P. M. (1998). Geostatistics and remote sensing. *Progress in Physical Geography*, *22*(1), 61–78. http://doi.org/10.1191/030913398667999161

Efros, A. A., & Freeman, W. T. (2001). Image quilting for texture synthesis and transfer. In *Proceedings of the 28th annual conference on Computer graphics and interactive techniques - SIGGRAPH '01* (pp. 341–346). Los Angeles, USA: ACM Press. http://doi.org/10.1145/383259.383296

Egbers, R. (2016). *Sentinel-2 data processing and identifying glacial features in Sentinel-2 imagery*. University of Technology.

El Ouassini, A., Saucier, A., Marcotte, D., & Favis, B. D. (2008). A patchwork approach to stochastic simulation: A route towards the analysis of morphology in multiphase systems. *Chaos, Solitons & Fractals*, *36*(2), 418–436. http://doi.org/10.1016/j.chaos.2006.06.100

Eldhuset, K., Andersen, P. H., Hauge, S., Isaksson, E., & Weydahl, D. J. (2003). ERS tandem InSAR processing for DEM generation, glacier motion estimation and coherence analysis on Svalbard. *International Journal of Remote Sensing*, *24*(7), 1415–1437. http://doi.org/10.1080/01431160210153039

ESA. (2013a). *Sentinel-1 User Handbook*. Paris: European Space Agency (ESA), European Commission. Retrieved from https://sentinel.esa.int/

ESA. (2013b). *Sentinel-1 User Handbook* (Vol. 1). Paris. Retrieved from https://sentinel.esa.int/

ESA. (2014). Introducing Sentinel-1. Retrieved June 1, 2016, from http://www.esa.int/Our_Activities/Observing_the_Earth/Copernicus/Sentinel-1/Introducing_Sentinel-1

ESA. (2016). Science Toolbox Exploitation Platform (SNAP). Retrieved January 1, 2016, from http://step.esa.int/main/toolboxes/snap/

Eskandari, K., & Srinivasan, S. (2008). Growthsim – A Multiple Point Framework for Pattern Simulation. In *7Th International Conference and Exposition on Petroleum Geophysics* (p. 4 pages). Hyderabad.

Fadlelmula, M. M., Killough, J., & Fraim, M. (2016). TiConverter: A training image converting tool for multiple-point geostatistics. *Computers & Geosciences*, *96*, 47–55. http://doi.org/10.1016/j.cageo.2016.07.002

Farr, T. G., & Kobrick, M. (2000). Shuttle radar topography mission produces a wealth of data. *Eos, Transactions American Geophysical Union*, *81*(48), 583. http://doi.org/10.1029/EO081i048p00583

Fatland, D. R., & Lingle, C. S. (1998). Analysis of the 1993-95 Bering Glacier (Alaska) surge using differential SAR interferometry. *Journal of Glaciology*, *44*(148), 532–546.

Fischer, A., Rott, H., & Björnsson, H. (2003). Observation of recent surges of Vatnajökull, Iceland, by means of ERS SAR interferometry. *Annals of Glaciology*, *37*(1), 69–76. http://doi.org/10.3189/172756403781815546

Furuya, M., & Wahr, J. M. (2005). Water level changes at an ice-dammed lake in west Greenland inferred from InSAR data. *Geophysical Research Letters*, *32*(14), 1–4. http://doi.org/10.1029/2005GL023458

Gabriel, A. K., Goldstein, R. M., & Zebker, H. A. (1989). Mapping small elevation changes over large areas: Differential radar interferometry. *Journal of Geophysical Research*, *94*(B7), 9183. http://doi.org/10.1029/JB094iB07p09183

Ge, Y., & Bai, H. (2011). Multiple-point simulation-based method for extraction of objects with spatial structure from remotely sensed imagery. *International Journal of Remote Sensing*, *32*(8), 2311–2335. http://doi.org/10.1080/01431161003698278

Gens, R., & Genderen, J. L. van. (1996). Analysis of the geometric parameters of SAR interferometry for spaceborne systems. In *International Archives of Photogrammetry and Remote Sensing* (pp. 107–110). Vienna, Austria.

Goldstein, R. M., Engelhardt, H., Kamb, B., & Frolich, R. M. (1993). Satellite Radar Interferometry for Monitoring Ice Sheet Motion: Application to an Antarctic Ice Stream. *Science*, *262*, 1525–1530.

Goldstein, R. M., & Werner, C. L. (1998). Radar interferogram filtering for geophysical applications. *Geophysical Research Letters*, *25*(21), 4035–4038. http://doi.org/10.1029/1998GL900033

González, P. J., Fernández, J., & Camacho, A. G. (2009). Coseismic three-dimensional displacements determined Using SAR data: Theory and an application test. *Pure and Applied Geophysics*, *166*(8–9), 1403–1424. http://doi.org/10.1007/s00024-009-0500-7

Goovaerts, P. (1997). *Geostatistics for natural resources evaluation*. Oxford, U. K.: Oxford University Press.

Gray, L., Joughin, I., Tulaczyk, S., Spikes, V. B., Bindschadler, R., & Jezek, K. (2005). Evidence for subglacial water transport in the West Antarctic Ice Sheet through three-dimensional satellite radar interferometry. *Geophysical Research Letters*, *32*(3), L03501. http://doi.org/10.1029/2004GL021387

Guardiano, F., & Srivastava, R. (1993). Multivariate Geostatistics - Beyond Bivariate Moments. In A. Soares (Ed.), *Quantitative Geology and Geostatistics* (Vol. 5, pp. 133–144). Troia.

Hamm, N. A. S., Finley, A. O., Schaap, M., & Stein, A. (2015). A spatially varying coefficient model for mapping PM10 air quality at the European scale. *Atmospheric Environment*, *102*, 393–405. http://doi.org/10.1016/j.atmosenv.2014.11.043

Hanssen, R. F. (2001). Radar Interferometry - Data Interpretation and Error Analysis. *Springer Science & Business Media (Vol. 2)*. Houten, The Netherlands. Retrieved from http://classes.images.alaska.edu/geos676/pdf/Massonnet_and_Feigl_1998.pdf

Higuchi, K., Watanabe, O., Fushimi, H., Takenaka, S., & Nagoshi, A. (2010). *Glaciers of Asia - GLACIERS OF NEPAL - Glacier Distribution in the Nepal Himalaya with Comparisons to the Karakoram Range*. *Satellite Image Atlas of Glaciers of the World*.

Hijmans, R. J. (2016). raster: Geographic Data Analysis and Modeling. R package version 2.5-8. Retrieved from https://cran.r-project.org/package=raster

Hilley, G. E., Burgmann, R., Ferretti, A., Novali, F., & Rocca, F. (2004). Dynamics of Slow-Moving Landslides from Permanent Scatterer Analysis. *Science*, *304*(5679), 1952–1955. http://doi.org/10.1126/science.1098821

Isaaks, E. H., & Srivastava, R. M. (1989). *Applied Geostatistics*. New York: Oxford University Press.

Jha, S. K., Mariethoz, G., Evans, J. P., & McCabe, M. F. (2013). Demonstration of a geostatistical approach to physically consistent downscaling of climate modeling simulations. *Water Resources Research*, *49*(1), 245–259. http://doi.org/10.1029/2012WR012602

Johnston, K., Ver Hoef, J. M., Krivoruchko, K., & Lucas, N. (2001). *Using ArcGIS geostatistical analyst. ESRI*. Redlands. Retrieved from http://direitosminerarios.com/pdf/ESRI - Using ArcGIS Geostatistical Analyst.pdf

Jónsson, S., Adam, N., & Björnsson, H. (1998). Effects of subglacial geothermal activity observed by satellite radar interferometry. *Geophysical Research Letters*, *25*(7), 1059. http://doi.org/10.1029/98GL50567

Joughin, I., Gray, L., Bindschadker, R., Price, S., Morse, D., Hulbe, C., … Werner, C. (1999). Tributaries of West Antarctic Ice Streams Revealed by RADARSAT Interferometry. *Science*, *286*(October), 283–286. http://doi.org/10.1126/science.286.5438.283

Joughin, I., Smith, B. E., & Abdalati, W. (2010). Glaciological advances made with interferometric synthetic aperture radar. *Journal of Glaciology*, *56*(200), 1026–1042. http://doi.org/10.3189/002214311796406158

Joughin, I., Winebrenner, D., Fahnestock, M., Kwok, R., & Krabill, W. (1996). Estimation of ice-sheet motion using satellite radar interferometry: method and error analysis with application to Humbolt Glacier, Greenland. *J. Glaciol.*, *42*(January 1996), 564–575. http://doi.org/http://dx.doi.org/10.3198/1996JoG42-142-564-575

Joughin, I., Winebrenner, D., Fahnestock, M., Kwok, R., & Krabill, W. (1996). Measurement of ice-sheet topography using satellite-radar interferometry. *Journal of Glaciology*, *42*(13), 10–22. http://doi.org/https://doi.org/10.3198/1996JoG42-140-10-22

Journel, A. G., & Huijbregts, C. J. (2003). *Mining Geostatistics*. London: Blackburn Press.

Journel, A., & Zhang, T. (2007). The Necessity of a Multiple-Point Prior Model. *Mathematical Geology*, *38*(5), 591–610. http://doi.org/10.1007/s11004-006-9031-2

Kääb, A. (2005). Combination of SRTM3 and repeat ASTER data for deriving alpine glacier flow velocities in the Bhutan Himalaya. *Remote Sensing of Environment*, *94*(4), 463–474. http://doi.org/10.1016/j.rse.2004.11.003

Kaltenborn, B. P., Nellemann, C., & Vistnes, I. I. (2010). *High mountain glaciers and climate change - Challenges to human livelihoods and adaptation*. *United Nations Environment Programme*. Retrieved from http://www.grida.no/_res/site/file/publications/glacier/himalayareport_screen.pdf

Karl, J. W. (2010). Spatial Predictions of Cover Attributes of Rangeland Ecosystems Using Regression Kriging and Remote Sensing. *Rangeland Ecology & Management*, *63*(3), 335–349. http://doi.org/10.2111/REM-D-09-00074.1

Kis, I. M. (2016). Comparison of Ordinary and Universal Kriging interpolation techniques on a depth variable (a case of linear spatial trend) , case study of the Šandrovac Field. *The Mining-Geology-Petroleum Engineering Bulletin*, 41–58. http://doi.org/10.17794/rgn.2016.2.4

König, M., Winther, J. G., & Isaksson, E. (2001). Measuring snow and glacier ice properties from satellite. *Reviews of Geophysics*, *39*(1), 1–27. http://doi.org/10.1029/1999RG000076

Kumar, V., Venkataraman, G., Rao, Y. S., Singh, G., & Snehmani. (2008). Spaceborne insar technique for study of himalayan glaciers using envisat asar and ers data. *International Geoscience and Remote Sensing Symposium (IGARSS)*, *4*(1), 1085–1088. http://doi.org/10.1109/IGARSS.2008.4779915

Kwok, R., & Fahnestock, M. A. (1996). Ice sheet motion and topography from radar interferometry. *IEEE Transactions on Geoscience and Remote Sensing*, *34*(1), 189–200. http://doi.org/10.1109/36.481903

Langley, K., Hamran, S. E., Hogda, K. A., Storvold, R., Brandt, O., Hagen, J. O., & Kohler, J. (2007). Use of C-Band Ground Penetrating Radar to Determine Backscatter Sources Within Glaciers. *IEEE Transactions on Geoscience and Remote Sensing*, *45*(5), 1236–1246. http://doi.org/10.1109/TGRS.2007.892600

Lee, J., Pottier, E., & Thompson, B. J. (2009). *Polarimetric Radar Imaging: From Basics to Applications*. Baton Rouge: CRC Press.

Leibowitz, E. (2009). Ten Interesting Facts about Glaciers | Blog Posts | WWF. Retrieved August 20, 2016, from http://www.worldwildlife.org/blogs/good-nature-travel/posts/ten-interesting-facts-about-glaciers

Li, M., Liew, S. C., & Kwoh, L. K. (2004). Automated production of cloudfree and cloud shadow-free image mosaics from cloudy satellite imagery. In *Proceedings of the 20th Congress International Society of Photogrammetry and Remote Sensing* (pp. 15–23). Retrieved from http://www.isprs.org/proceedings/XXXV/congress/comm3/papers/369.pdf

Li, S., Benson, C., Gens, R., & Lingle, C. (2008). Motion patterns of Nabesna Glacier (Alaska) revealed by interferometric SAR techniques. *Remote Sensing of Environment*, *112*(9), 3628–3638. http://doi.org/10.1016/j.rse.2008.05.015

Li, S., & Sturm, M. (2002). Patterns of wind-drifted snow on the Alaskan arctic slope, detected with ERS-1 interferometric SAR. *Journal of Glaciology*, *48*(163), 495–504. http://doi.org/10.3189/172756502781831151

Lu, Z., Fielding, E., Patrick, M. R., & Trautwein, C. M. (2003). Estimating lava volume by precision combination of multiple baseline spaceborne and airborne interferometric synthetic aperture radar: the 1997 eruption of okmok volcano, alaska. *IEEE Transactions on Geoscience and Remote Sensing*, *41*(6), 1428–1436. http://doi.org/10.1109/TGRS.2003.811553

Luckman, A., Quincey, D., & Bevan, S. (2007). The potential of satellite radar interferometry and feature tracking for monitoring flow rates of Himalayan glaciers. *Remote Sensing of Environment*, *111*(2–3), 172–181. http://doi.org/10.1016/j.rse.2007.05.019

Mahmud, K., Mariethoz, G., Caers, J., Tahmasebi, P., & Baker, A. (2014). Simulation of Earth textures by conditional image quilting. *Water Resources Research*, *50*(4), 3088–3107. http://doi.org/10.1002/2013WR015069

Mair, D., Nienow, P., Willis, I., & Sharp, M. (2001). Spatial patterns of glacier motion during a high-velocity event: Haut Glacier d'Arolla, Switzerland. *Journal of Glaciology*, *47*(156), 9–20. http://doi.org/10.3189/172756501781832412

Makkeasorn, A., Chang, N. B., Beaman, M., Wyatt, C., & Slater, C. (2006). Soil moisture estimation in a semiarid watershed using RADARSAT-1 satellite imagery and genetic programming. *Water Resources Research*, *42*(9), W09401. http://doi.org/10.1029/2005WR004033

Malvic, T., & Balic, D. (2009). Linearity and Lagrange Linear Multiplicator in the Equations of Ordinary Kriging. *Nafta: Exploration, Production, Processing, Petrochemistry*, *60*(1), 31–43.

Mariethoz, G. (2009). Geological Stochastic Imaging for Aquifer Characterization (p. 225). Neuchâtel, Switzerland: Pd. D. Dissertation, Université de Neuchâtel.

Mariethoz, G., & Caers, J. (2015). *Multiple-point geostatistics stochastic modeling with training images* (first). Wiley-Blackwell.

Mariethoz, G., & Kelly, B. F. J. (2011). Modeling complex geological structures with elementary training images and transform-invariant distances. *Water Resources Research*, *47*(7), W07527. http://doi.org/10.1029/2011WR010412

Mariethoz, G., Linde, N., Jougnot, D., & Rezaee, H. (2015). Feature-preserving interpolation and filtering of environmental time series. *Environmental Modelling & Software*, *72*, 71–76. http://doi.org/10.1016/j.envsoft.2015.07.001

Mariethoz, G., McCabe, M. F., & Renard, P. (2012). Spatiotemporal reconstruction of gaps in multivariate fields using the direct sampling approach. *Water Resources Research*, *48*(10), W10507. http://doi.org/10.1029/2012WR012115

Mariethoz, G., & Renard, P. (2010). Reconstruction of Incomplete Data Sets or Images Using Direct Sampling. *Mathematical Geosciences*, *42*(3), 245–268. http://doi.org/10.1007/s11004-010-9270-0

Mariethoz, G., Renard, P., & Straubhaar, J. (2010). The Direct Sampling method to perform multiple-point geostatistical simulations. *Water Resources Research*, *46*(11), W11536. http://doi.org/10.1029/2008WR007621

Massonnet, D., Briole, P., & Arnaud, A. (1995). Deflation of Mount Etna monitored by spaceborne radar interferometry. *Nature*, *375*(6532), 567–570. http://doi.org/10.1038/375567a0

Massonnet, D., & Feigl, K. L. (1998). Radar interferometry and its application to changes in the Earth's surface. *Reviews of Geophysics*, *36*(4), 441–500. http://doi.org/10.1029/97RG03139

Massonnet, D., Rossi, M., Carmona, C., Adragna, F., Peltzer, G., Feigl, K., & Rabaute, T. (1993). The displacement field of the Landers earthquake mapped by radar interferometry. *Nature*, *364*(6433), 138–142. http://doi.org/10.1038/364138a0

Mattar, K. E., Gray, A. L., Geudtner, D., & Vachon, P. W. (1999). Interferometry for DEM and Terrain Displacement: Effects of Inhomogeneous Propagation. *Canadian Journal of Remote Sensing*, *25*(1), 60–69. http://doi.org/10.1080/07038992.1999.10855263

Mattar, K. E., Vachon, P. W., Geudtner, D., Gray, A. L., Cumming, I. G., & Brugman, M. (1998). Validation of alpine glacier velocity measurements using ERS Tandem-Mission SAR data. *IEEE Transactions on Geoscience and Remote Sensing*, *36*(3), 974–984. http://doi.org/10.1109/36.673688

Meerschman, E., Pirot, G., Mariethoz, G., Straubhaar, J., Van Meirvenne, M., & Renard, P. (2013). A practical guide to performing multiple-point statistical simulations with the Direct Sampling algorithm. *Computers and Geosciences*, *52*, 307–324. http://doi.org/10.1016/j.cageo.2012.09.019

Mohr, J. J., & Madsen, S. N. (2000). Processing interferometric ERS-1/2 tandem data coast to coast in

Greenland. In *ERS-ENVISAT Symposium*. Gothenburg, Sweden.

Mohr, J. J., Reeh, N., & Madsen, S. N. (1998). Three-dimensional glacial flow and surface elevation measured with radar interferometry. *Nature*, *391*(6664), 273–276. http://doi.org/10.1038/34635

Mool, P. K., Maskey, P. R., Koirala, A., Joshi, S. P., Wu, L., Shrestha, A. B., … Shrestha, R. B. (2011). *Glacial Lakes and Glacial Lake Outburst Floods in Nepal. Icimod.*

Muskett, R. R., Lingle, C. S., Sauber, J. M., Rabus, B. T., & Tangborn, W. V. (2008). Acceleration of surface lowering on the tidewater glaciers of Icy Bay, Alaska, U.S.A. from InSAR DEMs and ICESat altimetry. *Earth and Planetary Science Letters*, *265*(3–4), 345–359. http://doi.org/10.1016/j.epsl.2007.10.012

Mustapha, H., & Dimitrakopoulos, R. (2011). HOSIM: A high-order stochastic simulation algorithm for generating three-dimensional complex geological patterns. *Computers & Geosciences*, *37*(9), 1242–1253. http://doi.org/10.1016/j.cageo.2010.09.007

Nagler, T., Rott, H., Hetzenecker, M., Wuite, J., & Potin, P. (2015). The Sentinel-1 Mission: New Opportunities for Ice Sheet Observations. *Remote Sensing*, *7*(7), 9371–9389. http://doi.org/10.3390/rs70709371

Olea, R. A., & Pawlowsky, V. (1996). Compensating for Estimation Smoothing in Kriging. *Mathematical Geology*, *28*(4), 407–417. http://doi.org/10.1007/BF02083653

Oriani, F., Straubhaar, J., Renard, P., & Mariethoz, G. (2014). Simulation of rainfall time series from different climatic regions using the direct sampling technique. *Hydrology and Earth System Sciences*, *18*(8), 3015–3031. http://doi.org/10.5194/hessd-11-3213-2014

Oveisgharan, S. (2007). Estimating Snow Accumulation From. *Group*, *45*(September), 129. http://doi.org/10.1109/TGRS.2006.886196

Papathanassiou, K., & Cloude, S. R. (2014). Single vs Multi-Polarization Interferometry. Retrieved November 22, 2016, from http://earth.esa.int/landtraining07/pol-insar_basic_concepts.pdf

Pebesma, E. J. (2004). Multivariable geostatistics in S: the gstat package. *Computers & Geosciences*, *30*(7), 683–691. http://doi.org/10.1016/j.cageo.2004.03.012

Pebesma, E. J., & Bivand, R. S. (2005). *Classes and methods for spatial data in R. R News* (Vol. 5). Retrieved from http://cran.r-project.org/doc/Rnews/

Peralvo, M., & Maidment, D. (2003). Influence of DEM interpolation methods in drainage analysis. *GIS Hydro*, 26. Retrieved from http://www.crwr.utexas.edu/gis/gishydro04/Introduction/TermProjects/Peralvo.pdf

Peredo, O., & Ortiz, J. M. (2011). Parallel implementation of simulated annealing to reproduce multiple-point statistics. *Computers and Geosciences*, *37*(8), 1110–1121. http://doi.org/10.1016/j.cageo.2010.10.015

Perski, Z., Jania, J., & Stober, M. (2004). SAR-interferometric flow velocities of two tidewater glaciers in NW Spitsbergen: Methods and results. In *FRINGE 2003 Workshop* (pp. 241–246). Frascati, Italy.

Petrakov, D., Shpuntova, A., Aleinikov, A., Kääb, A., Kutuzov, S., Lavrentiev, I., … Usubaliev, R. (2016). Accelerated glacier shrinkage in the Ak-Shyirak massif, Inner Tien Shan, during 2003–2013. *Science of The Total Environment*, *562*, 364–378. http://doi.org/10.1016/j.scitotenv.2016.03.162

Prats-Iraola, P., Nannini, M., Scheiber, R., De Zan, F., Wollstadt, S., Minati, F., … Desnos, Y.-L. (2015). Sentinel-1 assessment of the interferometric wide-swath mode. *Proceedings of the IEEE International Geoscience and Remote Sensing Symposium*, 5247–5251. http://doi.org/10.1109/IGARSS.2015.7327018

Quincey, D. J., Luckman, A., & Benn, D. (2009). Quantification of Everest region glacier velocities between 1992 and 2002, using satellite radar interferometry and feature tracking. *Journal of Glaciology*, *55*(192), 596–606. http://doi.org/10.3189/002214309789470987

Quincey, D. J., Richardson, S. D., Luckman, A., Lucas, R. M., Reynolds, J. M., Hambrey, M. J., & Glasser, N. F. (2007). Early recognition of glacial lake hazards in the Himalaya using remote sensing datasets. *Global and Planetary Change*, *56*(1–2), 137–152. http://doi.org/10.1016/j.gloplacha.2006.07.013

R Core Team. (2016). R: A language and environment for statistical computing. Vienna, Austria: R Foundation for Statistical Computing. Retrieved from https://www.r-project.org/

Remy, N. (2005). S-GeMS: The Stanford Geostatistical Modeling Software: A Tool for New Algorithms Development. In O. Leuangthong & C. V. Deutsch (Eds.), *Geostatistics Banff 2004* (pp. 865–871). Dordrecht: Springer Netherlands. http://doi.org/10.1007/978-1-4020-3610-1_89

Remy, N., Boucher, A., & Wu, J. (2009). *Applied Geostatistics with SGeMS: A User's Guide*. *Applied Geostatistics with SGeMS*. New York, NY: Cambridge University Press.

Rezaee, H., Asghari, O., & Yamamoto, J. K. (2012). On the reduction of the ordinary kriging smoothing effect, *2*(2), 102–117.

Richardson, S. D., & Reynolds, J. M. (2000). An overview of glacial hazards in the Himalayas. *Quaternary International*, *65–66*, 31–47. http://doi.org/10.1016/S1040-6182(99)00035-X

Romeiser, R., Runge, H., Suchandt, S., Sprenger, J., Weilbeer, H., Sohrmann, A., & Stammer, D. (2007). Current Measurements in Rivers by Spaceborne Along-Track InSAR. *IEEE Transactions on Geoscience and Remote Sensing*, *45*(12), 4019–4031. http://doi.org/10.1109/TGRS.2007.904837

Rosen, P. A., Hensley, S., Joughin, I. R., Li, F. K., Madsen, S. N., Rodriguez, E., & Goldstein, R. M. (2000). Synthetic aperture radar interferometry. *Proceedings of the IEEE*, *88*(3), 333–382. http://doi.org/10.1109/5.838084

Rott, H. (2009). Advances in interferometric synthetic aperture radar (InSAR) in earth system science. *Progress in Physical Geography*, *33*(6), 769–791. http://doi.org/10.1177/0309133309350263

Rott, H., & Nagler, T. (2006). The contribution of radar interferometry to the assessment of landslide hazards. *Advances in Space Research*, *37*(4), 710–719. http://doi.org/10.1016/j.asr.2005.06.059

Rott, H., Stuefer, M., Siegel, A., Skvarca, P., & Eckstaller, A. (1998). Mass fluxes and dynamics of Moreno Glacier, Southern Patagonia Icefield. *Geophysical Research Letters*, *25*(9), 1407–1410. http://doi.org/10.1029/98GL00833

Schneevoigt, N. J., Sund, M., Bogren, W., Kääb, A., & Weydahl, D. J. (2012). Glacier displacement on Comfortlessbreen, Svalbard, using 2-pass differential SAR interferometry (DInSAR) with a digital elevation model. *Polar Record*, *48*(1), 17–25. http://doi.org/10.1017/S0032247411000453

Smith, L. C., Alsdorf, D. E., Magilligan, F. J., Gomez, B., Mertes, L. A. K., Smith, N. D., & Garvin, J. B. (2000). Estimation of erosion, deposition, and net volumetric change caused by the 1996 Skeiðarársandur jökulhlaup, Iceland, from Synthetic Aperture Radar Interferometry. *Water Resources Research*, *36*(6), 1583–1594. http://doi.org/10.1029/1999WR900335

Straubhaar, J. (2016). *DeeSse User ' s Guide*. The Centre for Hydrogeology and Geothermics (CHYN), University of Neuchâtel.

Straubhaar, J., Renard, P., Mariethoz, G., Froidevaux, R., & Besson, O. (2011). An Improved Parallel Multiple-point Algorithm Using a List Approach. *Mathematical Geosciences*, *43*(3), 305–328. http://doi.org/10.1007/s11004-011-9328-7

Strebelle, S. (2002). Conditional Simulation of Complex Geological Structures Using Multiple-Point Statistics. *Mathematical Geology*, *34*(1), 1–21. http://doi.org/10.1023/A:1014009426274

Strebelle, S., & Remy, N. (2005). Post-processing of multiple-point geostatistical models to improve reproduction of training patterns. In O. Leuangthong & V. Deutsch (Eds.), *Quantitative Geology and Geostatistics* (pp. 979–988). Banff, Canada.

Strozzi, T., Kouraev, A., Wiesmann, A., Wegmüller, U., Sharov, A., & Werner, C. (2008). Estimation of Arctic glacier motion with satellite L-band SAR data. *Remote Sensing of Environment*, *112*(3), 636–645. http://doi.org/10.1016/j.rse.2007.06.007

Strozzi, T., Luckman, A., Murray, T., Wegmuller, U., & Werner, C. L. (2002). Glacier motion estimation using SAR offset-tracking procedures. *IEEE Transactions on Geoscience and Remote Sensing*, *40*(11), 2384–2391. http://doi.org/10.1109/TGRS.2002.805079

Strozzi, T., Wegmuller, U., & Matzler, C. (1999). Mapping wet snowcovers with SAR interferometry. *International Journal of Remote Sensing*, *20*(12), 2395–2403. http://doi.org/10.1080/014311699212083

Strozzi, T., Wegmuller, U., Werner, C., Wiesmann, A., & Santoro, M. (2007). Potential of a C-band SAR mission with 12-day repeat cycle to derive ice surface velocity with interferometry and offset tracking. In *2007 IEEE International Geoscience and Remote Sensing Symposium* (pp. 4229–4232). IEEE. http://doi.org/10.1109/IGARSS.2007.4423784

Tahmasebi, P., Hezarkhani, A., & Sahimi, M. (2012). Multiple-point geostatistical modeling based on the cross-correlation functions. *Computational Geosciences*, *16*(3), 779–797. http://doi.org/10.1007/s10596-012-9287-1

Tamm, T., Zalite, K., Voormansik, K., & Talgre, L. (2016). Relating Sentinel-1 Interferometric Coherence to Mowing Events on Grasslands. *Remote Sensing*, *8*(10), 802. http://doi.org/10.3390/rs8100802

Tang, Y., Atkinson, P. M., Wardrop, N. A., & Zhang, J. (2013). Multiple-point geostatistical simulation for post-processing a remotely sensed land cover classification. *Spatial Statistics*, *5*(1), 69–84. http://doi.org/10.1016/j.spasta.2013.04.005

Thompson, S. S., Benn, D. I., Dennis, K., & Luckman, A. (2012). A rapidly growing moraine-dammed glacial lake on Ngozumpa Glacier, Nepal. *Geomorphology*, *145–146*, 1–11. http://doi.org/10.1016/j.geomorph.2011.08.015

Van der Meer, F. (2012). Remote-sensing image analysis and geostatistics. *International Journal of Remote Sensing*, *33*(18), 5644–5676. http://doi.org/10.1080/01431161.2012.666363

Vieli, A., Payne, A. J., Shepherd, A., & Du, Z. (2007). Causes of pre-collapse changes of the Larsen B ice shelf: Numerical modelling and assimilation of satellite observations. *Earth and Planetary Science Letters*, *259*(3–4), 297–306. http://doi.org/10.1016/j.epsl.2007.04.050

Wangensteen, B., Weydahl, D. J., & Hagen, J. O. (1999). Mapping glacier velocities at Spitsbergen using ERS tandem SAR data. *Geoscience and Remote Sensing Symposium, 1999. IGARSS'99 Proceedings. IEEE 1999 International*, *4*(January), 1954–1956. http://doi.org/10.1109/IGARSS.1999.774997

Wangensteen, B., Weydahl, D. J., & Hagen, J. O. (2005). Mapping glacier velocities on Svalbard using ERS tandem DInSAR data. *Norsk Geografisk Tidsskrift - Norwegian Journal of Geography*, *59*(4), 276–285. http://doi.org/10.1080/00291950500375500

Wdowinski, S. (2004). Space-based measurements of sheet-flow characteristics in the Everglades wetland, Florida. *Geophysical Research Letters*, *31*(15), L15503. http://doi.org/10.1029/2004GL020383

Webster, R., & Oliver, M. A. (2007). *Geostatistics for Environmental Scientists.* (V. Barnett, S. Senn, & M. Scoot, Eds.) (2nd ed., Vol. 1). Wiley.

Wegmuller, U., & Werner, C. (1997). Gamma SAR processor and interferometry software. In *Third ERS scientific symposium* (pp. 1687–1692). Florence, Italy: ESA SP-414.

Wegmüller, U., & Werner, C. (1997). Retrieval of vegetation parameters with SAR interferometry. *IEEE Transactions on Geoscience and Remote Sensing*, *35*(1), 18–24. http://doi.org/10.1109/36.551930

Woodcock, C. E., Strahler, A. H., & Jupp, D. L. B. (1988). The use of variograms in remote sensing: I. Scene models and simulated images. *Remote Sensing of Environment*, *25*(3), 323–348. http://doi.org/10.1016/0034-4257(88)90108-3

Wuite, J., Rott, H., Hetzenecker, M., Floricioiu, D., De Rydt, J., Gudmundsson, G. H., … Kern, M. (2015). Evolution of surface velocities and ice discharge of Larsen B outlet glaciers from 1995 to 2013. *Cryosphere*, *9*(3), 957–969. http://doi.org/10.5194/tc-9-957-2015

Yague-Martinez, N., Prats-Iraola, P., Gonzalez, F. R., Brcic, R., Shau, R., Geudtner, D., … Bamler, R. (2016). Interferometric Processing of Sentinel-1 TOPS Data. *IEEE Transactions on Geoscience and Remote Sensing*, *54*(4), 2220–2234. http://doi.org/10.1109/TGRS.2015.2497902

Yamamoto, J. K. (2005). Correcting the Smoothing Effect of Ordinary Kriging Estimates. *Mathematical Geology*, *37*(1), 69–94. http://doi.org/10.1007/s11004-005-8748-7

Yaseen, M., Hamm, N. A. S., Tolpekin, V. A., & Stein, A. (2013). Anisotropic kriging to derive missing coseismic displacement values obtained from synthetic aperture radar images. *Journal of Applied Remote Sensing*, *7*(1), 73580. http://doi.org/10.1117/1.JRS.7.073580

Yaseen, M., Hamm, N. A. S., Woldai, T., Tolpekin, V. A., & Stein, A. (2013). Local interpolation of coseismic displacements measured by InSAR. *International Journal of Applied Earth Observation and Geoinformation*, *23*(1), 1–17. http://doi.org/10.1016/j.jag.2012.12.002

Yin, G., Mariethoz, G., & McCabe, M. F. (2015). A Multiple-point Geostatistics Method for filling gaps in Landsat E TM + SLC-off images. In T. Weber, M. J. McPhee, & R. S. Anderssen (Eds.), *MODSIM2015, 21st International Congress on Modelling and Simulation* (pp. 180–186). Gold Coast, Australia: Modelling and Simulation Society of Australia and New Zealand. Retrieved from http://www.mssanz.org.au/modsim2015/A3/yin.pdf

Zebker, H. A., & Goldstein, R. M. (1986). Topographic mapping from interferometric synthetic aperture radar observations. *Journal of Geophysical Research*, *91*(B5), 4993. http://doi.org/10.1029/JB091iB05p04993

Zebker, H. A., & Villasenor, J. (1992). Decorrelation in interferometric radar echoes. *IEEE Transactions on Geoscience and Remote Sensing*, *30*(5), 950–959. http://doi.org/10.1109/36.175330

Zhang, C., Li, W., & Travis, D. J. (2009). Restoration of clouded pixels in multispectral remotely sensed imagery with cokriging. *International Journal of Remote Sensing*, *30*(9), 2173–2195. http://doi.org/10.1080/01431160802549294

Zhang, T., Switzer, P., & Journel, A. (2006). Filter-based classification of training image patterns for spatial simulation. *Mathematical Geology*, *38*(1), 63–80. http://doi.org/10.1007/s11004-005-9004-x

Zhang, X., Jiang, H., Zhou, G., Xiao, Z., & Zhang, Z. (2012). Geostatistical interpolation of missing data and downscaling of spatial resolution for remotely sensed atmospheric methane column concentrations. *International Journal of Remote Sensing*, *33*(1), 120–134. http://doi.org/10.1080/01431161.2011.584078

Zhou, X., Chang, N., & Li, S. (2009). Applications of SAR Interferometry in Earth and Environmental Science Research. *Sensors*, *9*(3), 1876–1912. http://doi.org/10.3390/s90301876

APPENDIX A: R CODES

In this appendix, the R codes used for file format conversion, accuracy assessment and OK are presented.

A.1 CONVERSION OF FILE FORMAT BETWEEN .GSLIB AND .TIF

```
#=====================================================
# CONVERSION BETWEEN .TIF INTO .GSLIB FORMAT
#=====================================================
library(raster)
rm(list=ls(all=TRUE))
setwd(Path)

# Input and output filenames and location
in_fname <- "GappedDisplacementMap.tif"
in_raster <- raster(in_fname)
out_fname <- "GappedDisplacementMap.gslib"

# Number of nodes
Nx <- in_raster@ncols                   # Number of columns in the .tif image
Ny <- in_raster@nrows                   # Number of rows in the .tif image
Nz <- 1                                 # Number of bands in the .tif image

# Scale in each dimension
Sx <- res(in_raster)[2]                 # Scale in the x-direction
Sy <- res(in_raster)[1]                 # Scale in the y-direction
Sz <- 1.0                               # Scale in the z-direction

# Origin coordinates
Ox <- in_raster@extent@xmin             # Origin in x-direction
Oy <- in_raster@extent@ymin             # Origin in y-direction
Oz <- 0.0                               # Origin in z-direction

nvar <- in_raster@file@nbands

# Variable names
varname1 <- "LOSdisplacement"
var1 <- values(in_raster)

l1 <- sprintf("%d %d %d %.2f %.2f %.2f %.2f %.2f %.2f",
        Nx, Ny, Nz, Sx, Sy, Sz, Ox, Oy, Oz)
l2 <- sprintf("%d", nvar)
```

```
#====================================================================
# CONVERSION OF .GSLIB INTO .TIF FORMAT (MULTIPLE SIMULATIONS)
#====================================================================
library(raster)
rm(list=ls(all=TRUE))
setwd(Path)

# Input and output filenames and locations
in_txtname <- "AvgTenSimulations.gslib"                # Input filename
in_imgname <- "GappedDisplacementMap.tif"              # Displacement map whose gaps were simulated
in_raster <- raster(in_imgname)
conn <- file(in_txtname, open="r")
in_lines <- readLines(conn)
close(conn)
varname <- "AvgTenSimulations"                         # Output filename
out_fname <- sprintf("%s.tif", varname)

nvar <- as.double(in_lines[2])

# Parse DN values
list_data <- (strsplit(in_lines[-(1:(nvar+2))], " "))
matrix_data <- matrix(unlist(list_data), ncol=nvar, byrow=TRUE)
class(matrix_data) <- "numeric"
average_data <- rowMeans(matrix_data)                  # Mean of simulations

# Overwrite values of the input raster
in_raster[ ] <- average_data
writeRaster(in_raster, out_fname, overwrite=TRUE)
```

A.2 BIVARIATE TI

```
#===============================================================
# CREATE BIVARIATE TI FROM TWO .TIF DISPLACEMENT MAPS INTO .GSLIB FORMAT
#===============================================================
setwd("Path")
library(raster)
rm(list=ls(all=TRUE))

# Input and output filename and location
# First input variable (Displacemnt map from Pair I)
in_fname <- "GappedDisplacementMap1.tif"
in_raster <- raster(in_fname)

# Second input variable (Displacement map from Pair II)
in_fname1 <- " GappedDisplacementMap2.tif"
in_raster1 <- raster(in_fname1)
out_fname <- "BivariateTI.gslib"

# Number of nodes
Nx <- in_raster@ncols                    # Number of columns in the .tif image
Ny <- in_raster@nrows                    # Number of rows in the .tif image
Nz <- 1                                  # Number of bands in the .tif image

# Scale in each dimension
Sx <- res(in_raster)[2]                  # Scale in the x-direction
Sy <- res(in_raster)[1]                  # Scale in the y-direction
Sz <- 1.0                                # Scale in the z-direction

# Origin coordinates
Ox <- in_raster@extent@xmin              # Origin in x-direction
Oy <- in_raster@extent@ymin              # Origin in y-direction
Oz <- 0.0                                # Origin in z-direction

nvar1 <- in_raster@file@nbands
nvar2 <- in_raster1@file@nbands
nvar <- nvar1 + nvar2

# Variable names
# Variable name 1
varname1 <- "LOSdisplacement1"
var1 <- values(in_raster)
# Variable name 2
varname2 <- "LOSdisplacement2"
var2 <- values(in_raster1)

l1 <- sprintf("%d %d %d %.2f %.2f %.2f %.2f %.2f %.2f",
        Nx, Ny, Nz, Sx, Sy, Sz, Ox, Oy, Oz)
l2 <- sprintf("%d", nvar)
datalines1 <- sprintf("%.6f %.6f", var1, var2)
f <- file(out_fname)
writeLines(c(l1, l2, varname1, varname2, datalines1), f)
close(f)
```

A.3 ACCURACY ASSESSMENT

```
#==========================================================
# ACCURACY ASSESSMENT (RMSE, SCATTERPLOTS, RESIDUALS HISTOGRAM)
#==========================================================
library(raster)
require(rgdal)

# Declare filenames
root <- "Path"
gapfname <- "gap142.shp"                 # Shapefile used to create the artificial gaps
layername <- "gap142"
origfname <- "DisplacementMap.tif"       # Original displacement map before imposing artificial gaps
simfname <- "AvgTenSimulations.tif"      # Simulated results in the artificial gaps

setwd(root)

# Extract values of original and simulated images overlapping the polygon shapefile with the gap info
gaps <- readOGR(dsn=gapfname, layer=layername)
orig <- raster(origfname)
simulated <- raster(simfname)
masked_orig <- unlist(extract(orig, gaps))
masked_simulated <- unlist(extract(simulated, gaps))

nodata <- -9999999                       # No data values used by DS

# Compute RMSE
deviations <- masked_simulated[masked_orig!=nodata] - masked_orig[masked_orig!=nodata]
n <- length(deviations[!is.na(deviations)])
# Print number of gapped pixels
sprintf("There are %d pixel gaps", n)
rmse <- sqrt(sum(deviations^2, na.rm=TRUE)/n)
me <- sum(deviations)/n

sprintf("The root mean square error is: %.7f", rmse)
sprintf("The mean error is: %.7f", me)

# Plot the histogram of the residuals in the artificial gaps
x11()
x <- deviations
h <- hist(x, breaks=100, col="dark blue", border="black",
     main="Histogram of error (DS - Pair I)", xlab = "Displacements (m)",
     xlim=c(-0.05, 0.05), axes = TRUE)

# Scatterplot of the reference and measured values with linear model
ref<-masked_orig[masked_orig!=nodata]            # Obtain reference values
mes<-masked_simulated[masked_orig!=nodata]       # Obtain simulated values
x11()
plot(mes, ref, main = "Linear Model of Reference ~ Predicted for DS-Pair I", xlab="Measured",
       ylab="Reference", pch=19, cex=0.2)
abline(lm(ref~mes), col="red")
```

A.4 ORDINARY KRIGING

```
#==============================================================
# CODES FOR ORDINARY KRIGING
#==============================================================
require(gstat)
require(sp)
library(raster)
require(rgdal)

rm(list=ls())
set.seed(22011989)

root <- "Path"
imgfname <- "GappedDisplacementMap.tif"          # Gapped displacement map derived from DInSAR
outfname <- "FilledDisplacementMap(OK).tif"      # Output (interpolation) filename

setwd(root)
gapraster <- raster(imgfname)
nodata <- -9999999                               # NoData values used by DS for gapped pixels

gaptable <- rasterToPoints(gapraster)
colnames(gaptable) <-  c("x", "y", "disp")
# Extract X and Y of missing values
missing.cells <- gaptable[gaptable[,3]==nodata, 1:2]
missing.cells <- as.data.frame(missing.cells)
coordinates(missing.cells) <- ~x + y
# Remove gaps and take a subset of samples
all.samples <- gaptable[gaptable[,3]!=nodata, ]
# Number of samples for variogram modelling
nsamples <- 6800
idx <- sample(1:nrow(all.samples), nsamples, replace=FALSE)
sub.samples <- all.samples[idx, ]
# Proportion of samples to be used for validation
valproportion <- 0.25
val.idx <- sample(1:nrow(sub.samples), nsamples*valproportion, replace=FALSE)
train.samples <- sub.samples[-val.idx, ]
val.samples <- sub.samples[val.idx, ]

train.samples <- as.data.frame(train.samples)
val.samples <- as.data.frame(val.samples)
coordinates(train.samples) <- ~x + y
coordinates(val.samples) <- ~x + y

# Histogram of the train sample data (calibrate the variogram model)
x11()
z <- train.samples$disp
h<-hist(z, breaks=25, col="gray64", xlab="Displacement (m)",
        main="Histogram of displacement with Normal Curve (Pair I)", axes = FALSE)
axis(side = 2, col.axis="black", pos = -0.2, las = 2, tck = -0.01)
axis(side = 1, col.axis="black", pos = 0, las = 0, tck = -0.01)
xfit<-seq(min(z),max(z),length=40)
yfit<-dnorm(xfit,mean=mean(z),sd=sd(z))
yfit <- yfit*diff(h$mids[1:2])*length(z)
lines(xfit, yfit, col="blue", lwd=2)
```

```
abline(v=median(z), col=3)
abline(v=mean(z), col=2)
legend("topright", lty = c(1, 1), col = c("red", "green"), legend = c("mean", "median"))

# Experimental Variogram modelling and fitting theoretical model
disp.ev <- variogram(disp~1, data=train.samples)
disp.ev
plot(disp.ev)
partial.sill <-  var(train.samples$disp)
model.type <- "Exp"                              # Theoretical model to be fitted to experimental variogram
range <- 4000
nugget <- 0
disp.mv <- fit.variogram(disp.ev,  model=vgm(partial.sill, model.type, range, nugget, fit.method=7))
str(disp.mv)
plot(disp.ev, disp.mv)

# Ordinary kriging to predict values at the gaps
disp.ok  <- krige(disp~1, loc=train.samples, newdata=missing.cells, model=disp.mv)
write(disp.ok, "OK_predictions")

# Plot kriged predictions and variance
X11()
spplot(disp.ok, "var1.pred", sp.layout=list("sp.points", pch=19, col="green", train.samples),
      main="Kriged predictions of Disp")
X11()
spplot(disp.ok, "var1.var", sp.layout=list("sp.points", pch=19, col="green", train.samples),
      main="Kriging variance of Disp")

# Validation
# Cross-validation
disp.cv <- krige.cv(disp~1, train.samples, model=disp.mv)
str(disp.cv)
me <- sum(disp.cv$residual) / length(disp.cv$residual)
mse <- sum(disp.cv$residual^2) / length(disp.cv$residual)
rmse <- sqrt(mse)
me
rmse

# Validate against separate dataset
disp.val.ok  <- krige(disp~1, loc=train.samples, newdata=val.samples, model=disp.mv)
# Calculate the mean error and RMSE
disp.err <- disp.val.ok$var1.pred - val.samples$disp
me <- sum(disp.err) / length(disp.err)
mse <- sum(disp.err^2) / length(disp.err)
rmse <- sqrt(mse)
me
rmse

# Rebuild the gapped image
gaptable[gaptable[,3]==nodata, 3] <- disp.ok@data[, 1]
predictedraster <- rasterFromXYZ(gaptable, res=res(gapraster), crs=crs(gapraster), digits=7)
writeRaster(predictedraster, outfname, overwrite=TRUE)
```